A Modified Cross-correlation Beamforming (MCBF) for Extracting Multimode Surface Wave Dispersion Curves from Ambient Seismic Noise

Tongwei Qin and Laiyu Lu*

Institute of Geophysics, China Earthquake Administration, Beijing, 100081, China

*Corresponding author: Laiyu Lu (laiyulu@cea-igp.ac.cn)

Key Points:

- A modified beamforming is proposed to extract multimode surface wave dispersion curves using short noise recordings
- The explicit relationship between cross-correlation beamforming and Frequency-Bessel transform is given
- An improved scheme is proposed to remove the aliasing artifacts, and its validity is demonstrated based on the synthetic and real data

Abstract

Beamforming (BF) and Frequency-Bessel transform (F-J) have been demonstrated to extract multimode surface wave dispersion curves from ambient seismic noise. F-J method implicitly assumes the structure under the array is laterally isotropic. As for the conventional BF method, although the azimuth-dependence phase velocity can be measured, the fictitious azimuth anisotropy created by array geometry would be projected into the result. In this paper, the weighted and modified cross-correlation beamforming (WCBF and MCBF) schemes are proposed to extract the multimode surface wave dispersion curves with sufficient resolution using quite short noise recordings. Compared with the conventional BF, only the plane waves with the azimuth consistent with the interstation orientations are considered in MCBF and the search over the incident plane waves from different azimuth is omitted. The azimuth-dependence velocity can therefore be extracted by MCBF, independent of the array geometry. As far as the measurement of azimuth-averaged velocity is concerned, we show that BF is equivalent with F-J. The explicit relationship between BF and F-J methods is derived. For the finite sampling in practical applications, the theoretical representations of the dispersion image generated by BF technique under different imaging conditions are given. These representations can be used to investigate analytically the features of the dispersion images in frequency-velocity domain and how the aliasing is eliminated by improved imaging condition. The proposed methods are validated for the synthetic data as well as the real data from the dense array at different scales.

Plain Language Summary

Benefiting from the advance of seismic interferometry technology, traditional array-based methods developed to process the data from the event or active source can be directly or redesigned to process the virtual source records. Beamforming (BF) and Frequency-Bessel transform (F-J) have been demonstrated to extract multimode surface wave dispersion curves from ambient seismic noise. Both methods assume that the structure beneath the array is laterally uniform. The weighted and modified cross-correlation beamforming (WCBF and MCBF) schemes are proposed in this paper. It was proved that multimode dispersion curves of surface wave can be measured by WCBF and MCBF with sufficient resolution using quite short noise recordings. Moreover, the azimuth-

dependence velocity can be extracted by MCBF, independent of the array geometry. The explicit relationships and equivalence between BF and F-J are proved as far as the application in extracting multimode dispersion curves is concerned. An improved imaging condition is suggested to remove the artificial aliasing based on the theoretical representations of MCBF for the finite sampling on spatial wavefield in practical applications. The proposed methods are validated for the synthetic data as well as the real data from the dense array at different scales.

1. Introduction

The theory of seismic interferometry (SI) suggests the Green's function can be retrieved by cross-correlating the seismic ambient noise recorded at two stations (Lobkis and Weaver, 2001; Campillo and Paul, 2003). That is, the records of a virtual source can be constructed by calculating the noise cross-correlation function (NCF) of the interstation. Benefiting from the advance in SI, as well as the deployment of large and dense arrays, array-based schemes such as spatial autocorrelation (SPAC) (Aki, 1957; Yamaya et al., 2021), Frequency-Bessel transform (F-J) (J. Wang et al., 2019) and beamforming (BF, or called CBF, cross-correlation beamforming) (Harmon et al., 2008; Roux and Ben-Zion, 2017; K. Wang et al., 2020), are proposed or redesigned to extract the multimode surface wave dispersion curves using ambient seismic noise. Compared with traditional noise-based two-station method, where the pure-path inversion is required after extracting the interstation dispersion curves, array-based method provides an opportunity to measure directly the lateral variation of the velocity using the subsets of the array (Roux and Ben-Zion, 2017; K. Wang et al., 2020). Another advantage of array-based methods over two-station surface wave method is their ability for extracting the multimode dispersion curves. The join of higher modes will increase the stability of the surface wave inversion and provide constraints on the deeper structure (Xia et al., 2003). Therefore, the array technology for extracting multimode surface wave dispersion with high accuracy using seismic ambient noise has attracted the attention of seismic community (Roux and Ben-Zion, 2017; J. Wang et al., 2019; K. Wang et al., 2020; Yamaya et al., 2021; Qin et al., 2022). Precise measurement of dispersion curves is the basis for high-resolution 3D S-wave velocity imaging using surface waves.

F-J method is rooted in the theoretical representation of the wavefield at the free surface of a layered model. For an isotropic layered model, the wavefield in the frequency domain at distance r can be written as the Fourier Bessel integral over wavenumber k (Harkrider, 1964; Ben-Menahem & Singh, 1968; Chen, 1999). The integral kernel is expressed as a fractional form related to the structure and source parameters. The surface wave is given by the integral contribution of the residues determined by the roots that make the denominator of the kernel vanish. The kernel can thereby be obtained by taking the inverse Fourier-Bessel transform over the propagation distance r. As a result, in frequency-velocity (f-v) or frequency-wavenumber (f-k) domain the peaks of the kernel would be associated with the eigenvalues of surface wave. Forbriger (2003) has applied Fourier-Bessel transform to extract dispersion curves of multimode Rayleigh wave using the seismogram gather at the surface excited by a hammer source. J. Wang et al. (2019) apply similar Fourier-Bessel transform to the records of the virtual source, and call it Frequency-Bessel (F-J) transform.

When F-J transform is used for virtual recordings, the fact that the eigenvalues of the surface waves are associated with the peaks in f-v or f-k domain can also be explained via the orthogonality of the Bessel functions. Taking the vertical component of Rayleigh waves as an example, the NCF in the time domain corresponds to the SPAC coefficient in the frequency domain(Chávez-García and Luzón, 2005; Tsai and Moschetti, 2010; Lu, 2021), i.e., the zero-order Bessel function $J_0(k_n r)$ of the first kind with argument $k_n r$, where k_n is the eigen-wavenumber of the Rayleigh wave and r is the interstation distance. F-J transform implies to compute the integral of $J_0(k_n r)J_0(kr)r$ over the distance r from 0 to infinite. Due to the orthogonality of the Bessel function, the F-J spectrogram would achieve a maximum at $k = k_n$. Considering this property, Hu et al. (2020) extends F-J to NCFs of cross components and to estimate dispersion curves of Love wave using the orthogonality of Bessel function with different orders. The artifacts caused by aliasing can be eliminated by considering only the waves propagating in one direction, replacing Bessel function with Hankel function, as done in Forbriger (2003), or by the modified F-J (Xi et al., 2021; Zhou and Chen, 2021). In practical application, all NCFs involved in the array at different azimuth are sorted according to their interstation distance. Treating NCFs as the virtual record propagated along a

supposed linear array, the F-J spectrogram is then obtained by implementing the F-J transform numerically. This means an azimuthally isotropic model is assumed. The velocity given by F-J transform is the azimuth-averaged result.

BF is another array-based method to estimate the phase velocity under the array (Harmon et al., 2008) using the ambient seismic noise. In terms of the azimuth-averaged phase velocity, BF is almost independent of the noise source and array configuration, and has already been successfully used in ChinArray with moving subarrays (K. Wang et al., 2020). Using the data from a dense array with interstation interval of about 1 km, Qin et al. (2022) proved that the multimode dispersion curves can also be extracted by BF. For the extraction of azimuth-averaged phase velocity, the assumption on lateral isotropy is made in BF, as done in F-J method. If the azimuthal anisotropy is an issue, BF can also give the phase velocity at different azimuth by picking the maximum of the beampower at that azimuth by omitting the summation over the azimuth (Löer et al., 2018). However, the azimuthal anisotropy obtained by conventional BF would be affected by noise sources and array configuration. The dominant orientation of the array distribution would be projected into the azimuthal anisotropy of the structure since the azimuth dependence of the artificial anisotropy caused by the station-pair orientation is consistent with the azimuth dependence of the surface wave velocity of the structure (Lu et al., 2018). Although the artificial anisotropy caused by the array geometry can be removed from the BF results (Lu et al., 2018), the additional process for correction may produce the uncertainty of the results. Moreover, the dispersion image given by conventional BF lacks clarity, especially at higher frequency range.

In this paper, the modified BF methods are proposed to extract the multimode dispersion curves of the surface wave from seismic ambient noise. Start from the conventional BF, we first correct the wavefield by multiplying $\sqrt{kr}$ to reduce the effect of geometric spread of the wave in high frequency range. We call this method as weighted cross-correlation beamforming (WCBF). Moreover, the modified cross-correlation beamforming (MCBF) is proposed to reduce the effect of the array geometry on the azimuthal anisotropy. An improved imaging condition of MCBF is suggested to remove the artificial aliasing. Another purpose of the paper is to present the relationship between BF and F-J. As the array-based technique, both methods deal with NCFs. In

BF method, the delay-and-sum of the time domain NCFs are calculated, although this is usually done in the frequency domain. In F-J method, the Fourier transform of NCFs, or the spatial wavefield represented by SPAC, is integrated over the interstation distance. Seismic interferometry theory shows that NCFs in the time domain and the SPAC expression in the frequency domain are two descriptions for the same physics (Chavez-Garcia and Luzon, 2005; Yokoi and Margaryan, 2008; Tsai and Moschetti, 2010; Lu, 2021). Therefore, we speculate there might be some connection between BF and F-J. An explicit expression of such a relationship is investigated in this paper.

The structure of the paper is as follows: the theory of the conventional BF is introduced and revisited in section 2. The proposed WCBF and MCBF are investigated in section 3 and section 4, respectively. Their relationships with F-J are also examined in these two sections. In section 5, the theoretical representations of MCBF are derived for a finite sampling in practical applications and an improved imaging condition is suggested to remove the artificial aliasing. The proposed methods are validated in section 6 based on the synthetic data as well as the field data from the dense array at different scales. The discussion and conclusions are given in section 7.

2. Revisiting the Theory on Beamforming

The beamforming was originally designed to estimate the predominant seismic wave, which would be body or surface wave. Initial application mainly focused on the detection of nuclear explosions (Lacoss et al., 1969; Picozzi et al., 2010), and were later applied to the waveform from earthquake and ambient seismic noise, usually used to investigate the back azimuth and slowness of the dominant signal or to obtain the velocity structure under the array. A brief review of BF is provided in this section, mainly focusing on the beamforming of seismic noise. Conventions used in this paper for Fourier transform, Hilbert transform and cross-correlation are given in Appendix A.

2.1. Conventional (Cross-correlation) Beamforming

The basic idea of beamforming is delay-and-sum. For the seismic surface wave or ambient noise, it is usually assumed a horizontal plane wave travelling over the array. The signal received at each station in the array is thought as the summation of the time-shifted plane wave. The beam trace can be expressed in the time domain as

$$b(\mathbf{s},t,\theta)=\frac{1}{N}\sum_{i=1}^{N}W_i d(\mathbf{x}_i,t+\tau_i) \tag{1}$$

where $d(\mathbf{x}_i,t)$ is the time series recorded at station $\mathbf{x}_i$. W_i is the weight. N is the number of stations involved in the array. $\mathbf{s}$ is the slowness vector of the incident plane wave with azimuth θ. $\tau_i=(\mathbf{x}_i-\mathbf{x}_0)\cdot\mathbf{s}$ is the time delay between station $\mathbf{x}_i$ and the reference position $\mathbf{x}_0$. Equation 1 can be written in frequency domain as,

$$b(\mathbf{k},\omega,\theta)=\frac{1}{N}\sum_{i=1}^{N}W_i d(\mathbf{x}_i,\omega)e^{-i\mathbf{k}\cdot(\mathbf{x}_i-\mathbf{x}_0)} \tag{2}$$

where $d(\mathbf{x}_i,\omega)$ is the Fourier transform of $d(\mathbf{x}_i,t)$.

The beampower $B(\mathbf{k},\omega,\theta)$ is usually taken as the beamforming output, which can be written as

$$B(\mathbf{k},\omega,\theta)=\left|b(\mathbf{k},\omega,\theta)\right|^2=\frac{1}{N^2}\left|\sum_{i=1}^{N}W_i D(\mathbf{x}_i,\omega)e^{-i\mathbf{k}\cdot(\mathbf{x}_i-\mathbf{x}_0)}\right|^2 \tag{3}$$

with

$$D(\mathbf{x}_i,\omega)=\frac{1}{L}d(\mathbf{x}_i,\omega) \tag{4}$$

where L is the signal length. Equation 3 can be recast into

$$\begin{aligned}B(\mathbf{k},\omega,\theta)&=\frac{1}{N^2}\left(\sum_{i=1}^{N}W_i D(\mathbf{x}_i,\omega)e^{-i\mathbf{k}\cdot(\mathbf{x}_i-\mathbf{x}_0)}\right)^*\left(\sum_{j=1}^{N}W_j D(\mathbf{x}_j,\omega)e^{-i\mathbf{k}\cdot(\mathbf{x}_j-\mathbf{x}_0)}\right)\\&=\frac{1}{N^2}\left(\sum_{i=1}^{N}\sum_{j=1}^{N}W_{ij}e^{i\mathbf{k}\cdot\mathbf{x}_i}C_{ij}(r_{ij},\omega)e^{-i\mathbf{k}\cdot\mathbf{x}_j}\right)\\&=\frac{1}{N^2}\left(\sum_{i=1}^{N}\sum_{j=1}^{N}W_{ij}C_{ij}(r_{ij},\omega)e^{-i\mathbf{k}\cdot(\mathbf{x}_j-\mathbf{x}_i)}\right)\\&=\frac{1}{N^2}\sum_{i=1}^{N}\sum_{j=1}^{N}W_{ij}C_{ij}(r_{ij},\omega)e^{-ikr_{ij}\cos(\theta_{ij}-\theta)}\end{aligned} \tag{5}$$

where

$$C_{ij}(r_{ij},\omega)=D^*(\mathbf{x}_i,\omega)D(\mathbf{x}_j,\omega)=\frac{1}{L^2}d^*(\mathbf{x}_i,\omega)d(\mathbf{x}_j,\omega) \tag{6}$$

is the cross spectral density matrix (CSDM) (e.g. Gerstoft and Tanimoto, 2007; Riahi et al., 2014) or cross-covariance matrix (e.g. Capon, 1969; Seydoux et al., 2017), in which the phase shift between

stations $\mathbf{x}_i$ and $\mathbf{x}_j$ is contained. r_{ij} and θ_{ij} denote the interstation distance and azimuth of the station pair, respectively. It can be found that Equation 3, which is derived based on the standard delay-and-sum beamforming, is identical to Equation 5, which can be obtained directly from the cross-spectral density matrix (Löer et al., 2018).

Löer et al. (2018) refers to Equations 3 or 5 as standard beamforming. Gal et al. (2019) call them conventional beamforming (or Bartlett beamforming). Ruigrok et al. (2017) call the beamforming shown in Equation 2 as conventional beamforming and the beamforming shown in Equation 5 as correlated beamforming (CBF). Meanwhile, they call the beamforming only considering the CSDM with $i \neq j$ as the cross-correlation beamforming (CCBF) since the autocorrelation is discarded. The definitions of CCBF and CBF are not distinguished in this paper. We refer to the beamforming shown in Equation 5 as the correlation beamforming (CBF) regardless of the autocorrelation is contained. Which correlation components are considered in calculation is determined by choosing the elements presented in the matrix CSDM, such as an upper triangular matrix, a lower triangular matrix or a matrix without diagonal elements.

2.2. Multimode Dispersion Image Obtained by CBF

To estimate the vector wavenumber $\mathbf{k}$ across the array, a search over all possible wavenumber and azimuth are performed in conventional BF. The beampower is calculated by fitting the CSDM between station $\mathbf{x}_i$ and $\mathbf{x}_j$ with a synthetic plane wave described by the vector wavenumber $\mathbf{k}$. Once the phase delay denoted by CSDM match the one required by the incident plane wave model, the constructive interference would occur and hence the summation shown in Equation 5 would reach a maximum. The slowness associated with the maximum gives the velocity of the structure under the array, and the corresponding azimuth associated with the maximum gives the direction of arrival (DOA) of the wave.

For surface waves, if more than one mode is incident as a plane wave at velocities with much difference, the multimode phase velocity can in principle be estimated by beamforming. This is more common at local scales, especially in sedimentary basins where the energy of higher modes is usually pronounced.

To generate the dispersion image in f-v domain, the beampower shown in Equation 5 for each frequency is calculated by

$$CBF(\mathbf{k},\omega,\theta)=\frac{1}{N^2}\left|\sum_{i=1}^{N}\sum_{j=1}^{N}C_{ij}\left(\mathbf{r}_{ij},\omega\right)e^{-i\mathbf{k}\cdot\mathbf{r}_{ij}}\right|. \tag{7}$$

Equation 7 and Equation 5 are theoretically equivalent except that the weight W_{ij} is ignored in Equation 7. In practical application, NCFs are usually asymmetric due to the complex source distribution. $C_{ij}(\mathbf{r}_{ij},\omega)$, the Fourier transform of NCFs, is not real. The modulus is therefore to be taken in Equation 7 as the beamforming output. The beampower is then averaged over θ. The dispersion image can thereby be obtained by combining the azimuth-averaged beampower of each frequency. We call Equation 7 as the conventional CBF for extraction of dispersion curves. K. Wang et al. (2020) have used CBF to estimate the azimuth-averaged phase velocity of the fundamental mode Rayleigh wave.

As an example, Figure 1 gives an illustration for extraction of multimode Rayleigh waves using CBF. Figure 1a shows the configuration of the array consisting of seventy-nine stations, which are sampled from the dense array located in Tongzhou with intervals of 1-2 km (Qin et al., 2022). Figure 1c shows the distribution of interstation distances as a function of azimuth. Figure 1b and 1d show the dispersion images. In Figure 1b, the beampower of each frequency is normalized by the maximum at that frequency. To highlight the energy along the dispersion branches at high frequencies, we normalize the difference between the beampower and the minimum at that frequency in Figure 1d. The fundamental mode (mode 0) and the first higher mode (mode 1) are observed in Figure 1d. Based on this CBF scheme, Qin et al. (2022) has successfully obtained the lateral variation of the phase velocity of these two modes. Note that Figure 1d is slightly different from Figure 5a in Qin et al. (2022) since different matrix elements of CSDM is used here to reduce the artifacts.

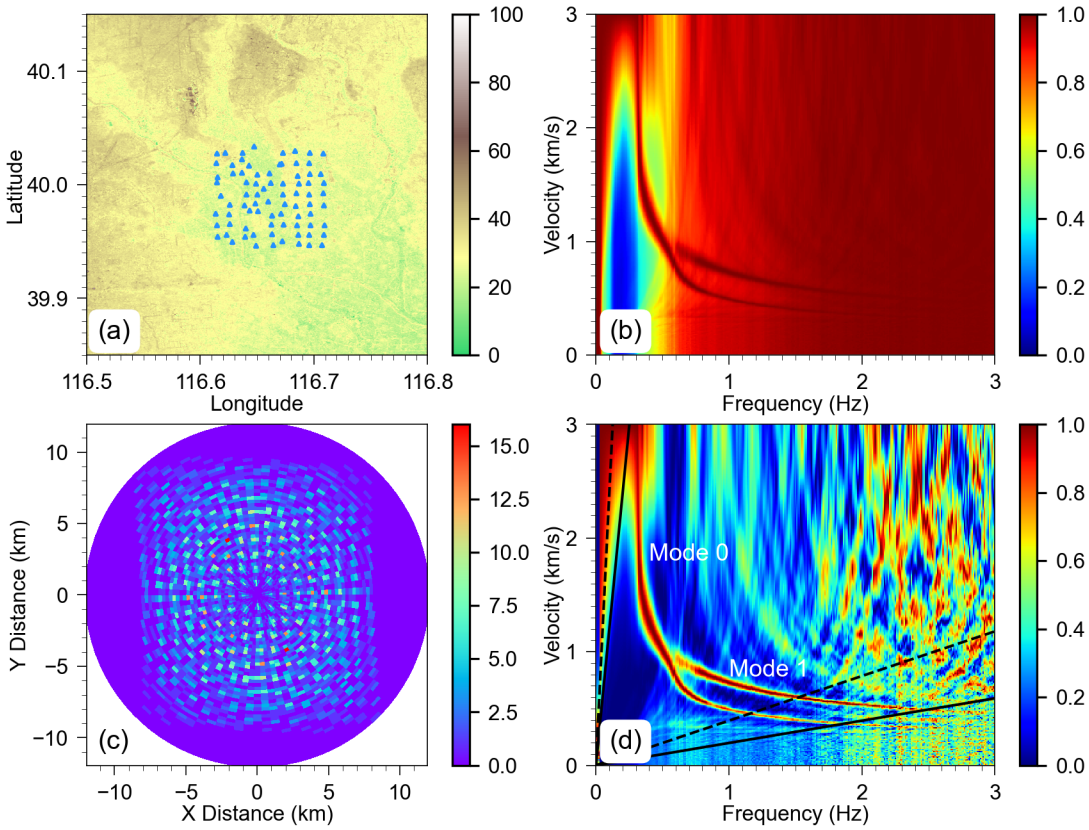

Figure 1. An illustration for the measurement of multimode surface wave by CBF. (a) The configuration of the array consisting of seventy-nine stations. (b) The azimuth-averaged dispersion image obtained by conventional CBF. For each frequency, the beampower is normalized by the maximum at that frequency. (c) The distribution of the number of station pairs as a function of the azimuth and interstation distance. (d) The same as (b) but with different normalized strategy. The dashed and solid black lines in (d) give the resolved wavenumber ranges estimated by $[k_{\min}, k_{\max}]$ and $[2k_{\min}, 2k_{\max}]$ using Equation 15, respectively.

2.3. Resolution and Aliasing of CBF

The resolution of BF depends on the array configuration and the characteristics of the wavefield across the array. The wavefield, for example the energy of the surface wave modes carried by the ambient noise, depends on the structure under the array and source characteristics which are often what we are trying to figure out. Therefore, the resolution we are concerned with and can be improved usually refers to the resolution determined by the array configuration.

The quantities appearing in Equation 7 are only related to the array configuration, except for the

CSDM which describes the wavefield. After removing CSDM, Equation 7 can be expressed as (Wathelet et al, 2008; Ruigork et al, 2017)

$$ARF(\mathbf{k}) = \frac{1}{N^2}\left|\sum_{i=1}^{N}\sum_{j=1}^{N} e^{-i\mathbf{k}\cdot\mathbf{r}_{ij}}\right| \tag{8}$$

Since

$$e^{-i\mathbf{k}\cdot(\mathbf{x}_j-\mathbf{x}_i)} = \left[e^{-i\mathbf{k}\cdot(\mathbf{x}_i-\mathbf{x}_j)}\right]^* \tag{9}$$

Equation 8 can also be written as (Horike 1985, Picozzi et al,2010)

$$ARF(\mathbf{k}) = \frac{1}{N^2}\sum_{i=1}^{N}\sum_{j=1}^{N} e^{-i\mathbf{k}\cdot(\mathbf{x}_j-\mathbf{x}_i)} \tag{10}$$

$ARF(\mathbf{k})$ is termed spatial window function (Lacoss et al, 1969; Horike 1985) or array response function (ARF) (Capon,1969; Rost and Thomas,2002; Ruigork et al, 2017).

For an incident monochromatic plane wave with given angular frequency ω_0 and wavenumber $\mathbf{k}_0$, by ignoring the attenuation, the CSDM between station $\mathbf{x}_i$ and $\mathbf{x}_j$ can be expressed as

$$C_{ij}(\omega) = \delta(\omega-\omega_0)e^{i\mathbf{k}_0\cdot(\mathbf{x}_j-\mathbf{x}_i)} \tag{11}$$

where $\delta(\omega-\omega_0)$ is the Dirac delta function. Substitute Equation 11 into Equation 5, the beamforming output for a monochromatic plane wave can be written as (Asten and Henstridge, 1984)

$$B(\omega,\mathbf{k}) = \left|W_f(\omega-\omega_0)\right|^2 ARF(\mathbf{k}-\mathbf{k}_0) \tag{12}$$

where $W_f(\omega-\omega_0)$ is the Fourier spectra of the time series with given limited length. For more general case, the estimated wavenumber spectrum is the 2D convolution of the true spectrum with ARF (Lacoss et al., 1969; Asten and Henstridge, 1984). The beamforming resolution is thereby controlled by ARF which depends on the array configuration.

At present, there is no global agreement about the capabilities of an array (Wathelet et al, 2008). For the array with simple and regular geometries, for instance, a linear array with equal spacing, the aliasing and resolution limit can be estimated by the maximum and minimum interstation spacing in the array using the Nyquist sampling theorem. For the array with irregular geometry,

some empirical rules are proposed to estimate the reasonable results achieved by the array. Tokimatsu (1997) use the minimum $r_{\min}$ and maximum $r_{\max}$ of the interstation distances inside the array to determine the range of the resolved wavelength. As a rule of thumb, the resolved minimum wavelength $\lambda_{\min}$ and maximum one $\lambda_{\max}$ are respectively $\lambda_{\min} = 2r_{\min}$ and $\lambda_{\max} = 3r_{\max}$.

A more rigorous definition for resolved wavenumber is based on ARF. For two plane waves travelling the array with wavenumbers $\mathbf{k}_1$ and $\mathbf{k}_2$, the CSDM can be expressed as

$$C_{ij}(r_{ij},\omega) = A_1(\omega)e^{i\mathbf{k}_1\cdot\mathbf{r}_{ij}} + A_2(\omega)e^{i\mathbf{k}_2\cdot\mathbf{r}_{ij}} \tag{13}$$

The f-k spectrum estimated from Equation 7 can be written as

$$\begin{aligned} CBF(\mathbf{k},\omega,\theta) &= \frac{1}{N^2}\left|\sum_{i=1}^{N}\sum_{j=1}^{N}\left(A_1(\omega)e^{i\mathbf{k}_1\cdot\mathbf{r}_{ij}} + A_2(\omega)e^{i\mathbf{k}_2\cdot\mathbf{r}_{ij}}\right)e^{-i\mathbf{k}\cdot\mathbf{r}_{ij}}\right| \\ &\le \frac{1}{N^2}\left(\left|\sum_{i=1}^{N}\sum_{j=1}^{N}A_1(\omega)e^{i\mathbf{k}_1\cdot\mathbf{r}_{ij}}e^{-i\mathbf{k}\cdot\mathbf{r}_{ij}}\right| + \left|\sum_{i=1}^{N}\sum_{j=1}^{N}A_2(\omega)e^{i\mathbf{k}_2\cdot\mathbf{r}_{ij}}e^{-i\mathbf{k}\cdot\mathbf{r}_{ij}}\right|\right) \\ &= \left|W_1(\omega-\omega_1)\right|^2 ARF(\mathbf{k}-\mathbf{k}_1) + \left|W_2(\omega-\omega_2)\right|^2 ARF(\mathbf{k}-\mathbf{k}_2) \end{aligned} \tag{14}$$

This means the beampower for two plane waves is always lower than the summation of individual plane waves (Wathelet et al., 2008). The aliasing and resolution of the array can be defined based on the ARF by considering the summation of two shifted ARFs. If two wavenumbers are close to each other, the summation of two shifted ARF would generate a wider main lobe rather than two narrow main lobes. The width of the main lobe of ARF which makes two wavenumbers cannot be distinguished is used to define the resolved wavenumber. The side lobes of two shifted ARFs may overlap and resulted the beampower with the same magnitude as the main lobe. The wavenumber associated with such overlapping sidelobes is defined as the aliasing wavenumber.

Figure 2a shows the ARF for the array shown in Figure 1a. The maximum occurred in the center at $\mathbf{k} = 0$. The aliasing is likely to occur at the wavenumbers where, for example, the four secondary peaks are observed, which appear in four typical directions around 0, 90, 180, 270 degrees. Figure 2b shows the cross sections of ARF every two degrees. Concerning on the resolution, the thinner is the central peak of ARF, the more capable is the array to distinguish two waves travelling at close wavenumbers (Wathelet et al., 2008). How to evaluate quantitatively the beamforming resolution

and the confidence interval that aliasing does not appear, different definitions are proposed by researchers. The wavenumber k_{Res} associated with the half-width of the main lobe, at the edge of which the beampower is reduced to a given threshold relative to the maximum, is usually used to define the resolving power of the wavenumber. As shown in Figure 2b, two wavenumbers cannot be resolved if their difference is less than $2k_{\mathrm{Res}}$ since two main lobes would overlap. If the maximum of the main lobe is 1, the threshold is generally selected as 0.5, i.e., the beampower reduces to the half of the maximum or -3dB in the logarithmic coordinates (Woods and Lintz,1973; Asten and Henstridge, 1984; Wathelet et al., 2008). For this definition, k_{Res} is equal to 0.34 Rad/km for the array shown in Figure 1a.

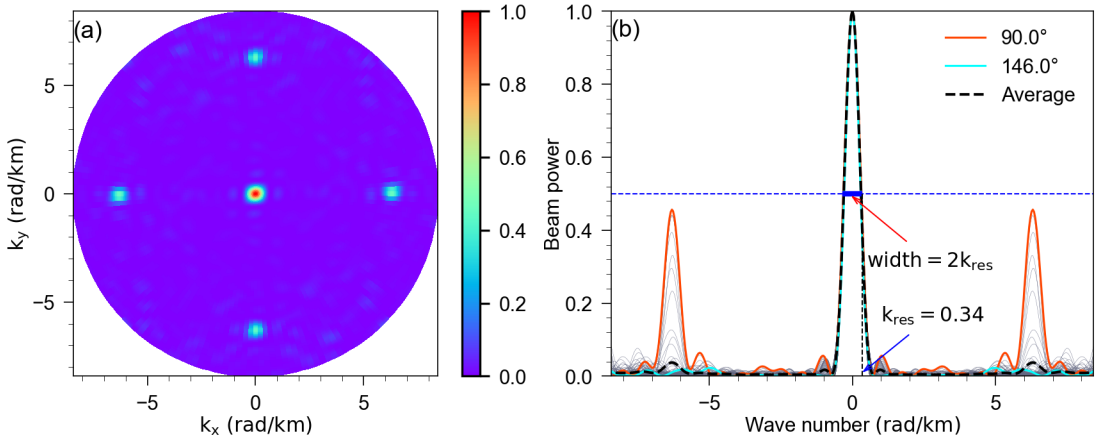

Figure 2. The array response function (ARF) for the array shown in Figure 1a. The gray lines in (b) denotes the cross sections of the ARF every two degrees. The black dashed line denotes the azimuth-averaged result. The blue dashed line denotes the location of 0.5 beampower.

On the other hand, based on the sampling theorem, the maximum ($k_{\max}$) and minimum ($k_{\min}$) wavenumbers that can be resolved by the array are

$$k_{\max} = \pi / r_{\min}$$
$$k_{\min} = \pi / r_{\max} \quad (15)$$

where $r_{\max}$ and $r_{\min}$ are the largest and smallest interstation distances, respectively. $k_{\max}$ is also called Nyquist wavenumber, the wavenumber exceeds which repetition would occur (e.g., see Figure 10). Ruigrok et al. (2017) also approximate the resolution using $k_{\min}$. For the array shown in Figure 1a, $k_{\max} = 15.98$ Rad/km, $k_{min} = 0.26$ Rad/km. By removing the aliasing in negative

frequency, the resolved wavenumber range would reach to $[2k_{\min}, 2k_{\max}]$. The dashed and solid black lines in Figure 1d gives the resolved wavenumber ranges estimated by $[k_{\min}, k_{\max}]$ and $[2k_{\min}, 2k_{\max}]$, respectively.

3. Weighted Cross-correlation Beamforming (WCBF)

It can be found from Figure 1b that for the conventional CBF, the energy difference around the eigenvalues from the ambient noise is not manifest at high frequencies. As a result, at the first glance in Figure 1b, the color scheme is different above and below 0.5 Hz, resulting the energy along the dispersion branches are not prominent for the frequencies above 0.5 Hz. This is mainly due to the attenuation and geometric spread of the wavefield at high frequencies. Of course, we can highlight the energy along the dispersive branches by changing the normalization strategy, as shown in Figure 1d. However, to correct the wavefield by multiplying $\sqrt{kr}$ in CBF is a natural alternative.

3.1. Correction of Wavenumber k and Propagation Distance r

Although representations are different literally, the conventional BF shown in Equation 3 and Equation 5 are actually equivalent. However, seismic interferometry endows Equation 5 with more physical explanations, which is not so obvious in Equation 3. The theory of seismic interferometry states that the Green's function can be retrieved by cross-correlating the seismic ambient noise. In the frequency domain, that is, the CSDM $C\left(\mathbf{x}_i, \mathbf{x}_j, \omega\right)$ is equivalent to the Green's function and can be represented as

$$C\left(\mathbf{x}_i, \mathbf{x}_j, \omega\right) = C_{ij}(\omega) \propto S(\omega)\,\mathrm{Im}\left[G\left(\mathbf{x}_i, \mathbf{x}_j, \omega\right)\right] \tag{16}$$

where $G\left(\mathbf{x}_i, \mathbf{x}_j, \omega\right)$ is the Green's function between $\mathbf{x}_i$ and $\mathbf{x}_j$. Due to the source distribution, the surface wave usually dominates the seismic noise. The Green's function in Equation 16 is therefore considered to be the surface wave Green's function. For the vertical component of a homogeneous layered medium, Equation 16 can be written as

$$C_{ij}(\omega) \propto S(\omega)\,\mathrm{Im}\left[G_{zz}\left(\mathbf{x}_i,\mathbf{x}_j,\omega\right)\right] = S(\omega)\,\mathrm{Re}\left[\sum_n \frac{1}{8cUI_1} r_2(n,\omega) r_1(n,\omega) H_0^{(2)}\left(k_n r_{ij}\right)\right] \tag{17}$$

where c is the phase velocity, U the group velocity. $r_1(z)$ and $r_2(z)$ are the radial and vertical eigen-function of the Rayleigh wave, respectively. $I_1 = \frac{1}{2}\int_0^\infty \rho\left(r_1^2 + r_2^2\right)dz$. n denotes the mode number. k_n is the horizontal wavenumber in the direction of r_{ij}. By expressing the Hankel function as the sum of the first and second kind of Bessel functions, Equation 17 can be recast as

$$C_{ij}(\omega) \propto S(\omega)\sum_n \frac{1}{8cUI_1} r_2(n,\omega) r_1(n,\omega) J_0\left(k_n r_{ij}\right) \tag{18}$$

This means, under the assumption of laterally homogeneous model and uniform distribution of noise source, the monochromatic wavefield across the array can be represented as $J_0(k_n r)$. This is consistent with the result on SPAC of the microtremor in the frequency domain, originally given by Aki (1957). Therefore, as a function of the interstation distance r, the Fourier transform of NCFs can be thought as the spatial sampling on a cylindrical wavefield described by the Bessel function $J_0\left(k_n r\right)$.

In the far field, $J_0\left(k_n r\right)$ can be expressed as

$$J_0\left(k_n r\right) \sim \sqrt{\frac{2}{\pi k_n r}}\cos\left(k_n r - \frac{\pi}{4}\right), k_n r \gg 0 \tag{19}$$

Figure 3a shows the variation of $J_0\left(k_n r\right)$ and its far field approximation as a function of the distance. If the weight W in Equation 5 is the same for all NCFs, the contribution of the NCFs with larger interstation distance or the wave with high frequency would be much smaller due to the spread factor $\sqrt{1/kr}$. This makes the mode recognition along dispersion branches lack clarity in high frequency range in Figure 1b. To improve the CBF results for larger $k_n r$, we correct the wavefield by considering the following weighted cross-correlation beamforming.

$$WCBF(\mathbf{k},\omega,\theta) = \frac{1}{N^2}\sum_{i=1}^{N}\sum_{j=1}^{N}\sqrt{|\mathbf{k}||\mathbf{r}_{ij}|}\,C_{ij}\left(\mathbf{r}_{ij},\omega\right)e^{i\mathbf{k}\cdot\mathbf{r}_{ij}} \tag{20}$$

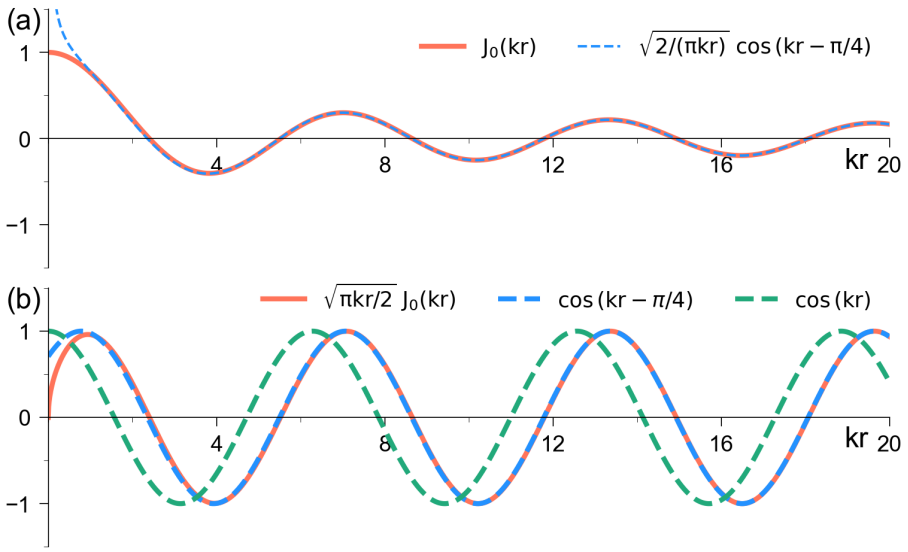

Figure 3. (a) The Bessel function $J_0\left(k_n r\right)$ and its far field approximation. (b) The amplitude modulated $J_0\left(k_n r\right)$ and cosine functions.

The variation of the corrected wavefield with the distance is shown in Figure 3b. The azimuth-averaged velocity is considered currently. The average over the azimuth implies to conduct the summation of Equation 20 over the angle θ, the azimuth of the wavenumber $\mathbf{k}$. This azimuth-averaged operation would again introduce a decay with a factor of $\sqrt{1/kr}$. Therefore, $\sqrt{kr}$ is again multiplied for the azimuth-averaged of Equation 20. It reads

$$\overline{WCBF}(k,\omega)=\frac{1}{N^2}\sum_{\theta=0}^{2\pi}\sum_{i=1}^{N}\sum_{j=1}^{N}kr_{ij}C_{ij}\left(\mathbf{r}_{ij},\omega\right)e^{ikr_{ij}\theta} \tag{21}$$

The overbar is used to denote the average over the azimuth. We call Equations 20 and 21 as the weighted cross-correlation beamforming (WCBF) since varying weight is adopted. Different from Equation 7, we take the real part of Equation 21 or its' absolute value as the imaging conditions for plotting, which are expressed as

$$\begin{aligned} WCBF1(k,\omega)&=\mathrm{Re}\left(\overline{WCBF}(k,\omega)\right)\\ WCBF2(k,\omega)&=\mathrm{ABS}\left[\mathrm{Re}\left(\overline{WCBF}(k,\omega)\right)\right] \end{aligned} \tag{22}$$

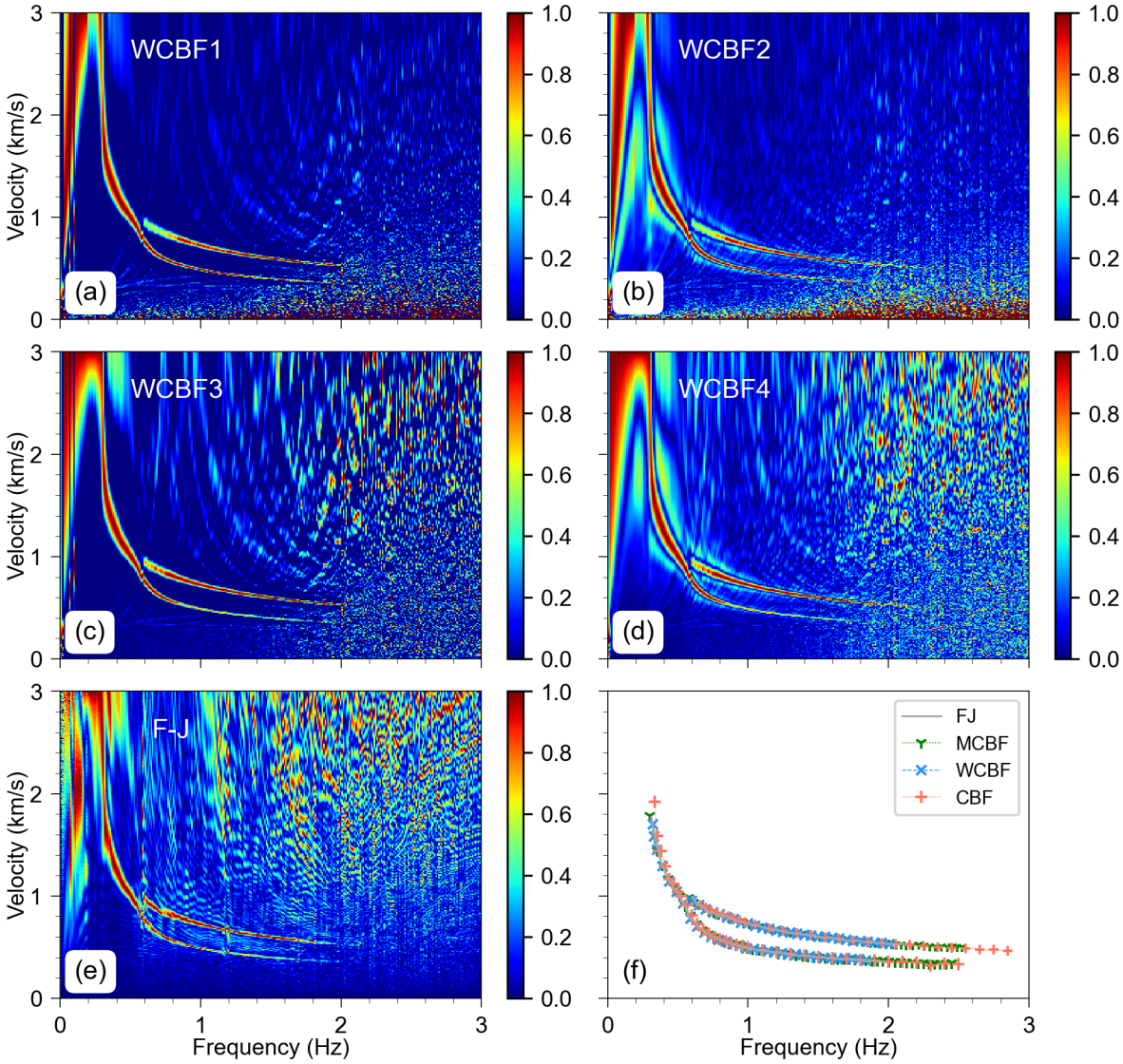

Figure 4. The dispersion images obtained by WCBF (a-d) and F-J (e). The comparison of the picked values from different methods are shown in (f). The gray lines in (f) show the F-J results picked from (e). The result of WCBF in (f) is picked from (a), which is the same as that from (b-d). The result of CBF in (f) is picked from Figure 1d.

Figures 4a and 4b show dispersion images in f-v domain calculated from Equation 22. The normalization strategy is the same as that used in Figure 1b. Figures 4a show the energy along two dispersion branches is more prominent than that in Figure 1b. The efficiency of the normalization strategy used in Figure 1d is achieved and exceeded by WCBF. Moreover, the dispersion images are much clearer in Figure 4a and 4b, and the artificial images occurred in the upper region with high velocities and frequencies in Figure 1d disappear. As a trade-off, at the lower of the panel,

some disturbing pixels appear around the area close to zero velocity. This would be caused by the overcorrection on the large wavenumber around zero velocity. These interfering pixels have little effect on mode recognition.

3.2. Relation Between WCBF and F-J

F-J is also an array-based method to extract the dispersion curves using ambient noise. In this section, the relation between WCBF and F-J is investigated. We start from the 2D Fourier transform of an arbitrary function. In polar coordinates, it can be expressed as (Baddour, 2011)

$$2\mathrm{DFFT}(k,\omega)=\frac{1}{2\pi}\int_0^{2\pi}\int_0^{+\infty}C_{ij}(r,\omega,\theta)e^{ikr\cos\theta}rdrd\theta \tag{23}$$

where $C_{ij}(r,\omega,\theta)$ can be an arbitrary function which depends on the azimuth θ and the radial distance r. It is assumed $C_{ij}(r,\omega,\theta)$ is independent of the azimuth. For instance, assuming it be the spectrum of the surface wave vertical component recorded at the surface of the laterally isotropic layered model, $C_{ij}(r,\omega,\theta)$ can be written as $C_{ij}(r,\omega)$. Since the Bessel function $J_0(kr)$ can be expressed as

$$J_0(kr)=\frac{1}{2\pi}\int_0^{2\pi}e^{ikr\cos\theta}d\theta \tag{24}$$

Equation 23 can then be rewritten as

$$2\mathrm{DFFT}(k,\omega)=FJ(k,\omega)=\frac{1}{2\pi}\int_0^{2\pi}\int_0^{+\infty}C_{ij}(r,\omega)e^{ikr\cos\theta}rdrd\theta=\int_0^{+\infty}C_{ij}(r,\omega)J_0(kr)rdr \tag{25}$$

Equation 25 is the F-J transform proposed by J. Wang et al (2019), which can be thought as the 2D Fourier transform of the radially symmetric function $C_{ij}(r,\omega)$. This implies the lateral isotropy is assumed for F-J method. Under this assumption, the 2D Fourier transform of the radially symmetric function is degenerated into the Fourier Bessel transform or Hankel transform.

The surface wave usually dominates the NCFs. As shown in Equation 18, for the vertical component, $C_{ij}(r,\omega)$ is related to the spatial autocorrelation coefficient $J_0(kr)$, i.e.,

$$C_{ij}(r,\omega)\sim S(\omega)J_0(k_nr) \tag{26}$$

Substituting Equation 26 into Equation 25 and considering the orthogonality of the Bessel function (Morse and Feshbach, 1953, P943), we have

$$FJ(k,\omega) = S(\omega)\int_0^{+\infty} J_0(k_n r)J_0(kr)rdr = S(\omega)\frac{\delta(k_n - k)}{k_n} \tag{27}$$

Consequently, the maxima in $\omega - k$ domain are associated with the eigenvalues k_n of the Rayleigh waves. The dispersion curves can then be measured by picking the velocities associated with the maxima in f-v domain.

Comparing Equations 25 and 21, it can be found that azimuth-averaged $\overline{WCBF}$ is the discrete form of F-J except for an extra wavenumber factor occurred in Equation 21. We define the new imaging conditions WCBF3 and WCBF4 by dividing Equation 22 by the wavenumber k. We have

$$\begin{aligned} WCBF3(k,\omega) &= \mathrm{Re}\left(\frac{1}{k}\overline{WCBF}(k,\omega)\right) = FJ(k,\omega) \\ WCBF4(k,\omega) &= \mathrm{ABS}\left[\mathrm{Re}\left(\frac{1}{k}\overline{WCBF}(k,\omega)\right)\right] \end{aligned} \tag{28}$$

The WCBF3 shown in Equation 28 is now equivalent to the F-J method. Compared with WCBF1 in Equation 22, only the propagation distance r is corrected in F-J method. Choosing $\sqrt{k}$ or $\sqrt{kr}$ to correct the wavefield is a trade-off that determines whether artifacts appear in the upper region with high velocities and frequencies, or in the lower region close to zero velocity. Figure 4c and 4d show the results calculated from Equation 28. As opposite to Figure 4a and 4b, the artifacts in Figure 4c and 4d appear in the upper region with higher velocities and frequencies. The disturbing pixels around the area close to zero velocity are significantly reduced. In addition, for the results of WCBF2 and WCBF4, where the absolute value of the real part is taken as the imaging condition, the apparent side lobes around the dispersion branches are observed in Figure 4b and 4d. Because the sampling of the array on the wavefield is always finite, Dirac delta function shown in Equation 27 would behave as a sinc function. The side lobes in Figure 4b and 4d originate from the negative values adjacent to the main lobe of the sinc function. They disappear in Figure 4a and 4c since only positive values are color-coded.

Figure 4e shows the result of F-J method. As expected, the dispersion image obtained by F-J method has the same characteristics as that of WCBF3 (Figure 4c). The slight difference possibly comes from the approximation of the numerical integration. An integral scheme based on the trapezoidal integration is used in F-J (J. Wang et al, 2019), while the discrete summation shown in

Equation 21, similar as the discrete Fourier summation, is used to directly compute the result of WCBF.

4. Modified Cross-correlation Beamforming (MCBF)

Different from the estimation on the azimuth-averaged velocity, the phase velocity as well as the azimuth associated with the maximum beampower are measured by CBF in Roux and Ben-Zion (2017). Admittedly, the azimuth-dependent velocity can be estimated by picking the values associated with the maximum beampower at that azimuth. The azimuthal anisotropy can then be estimated by fitting the model proposed by Smith and Dahlen (1973), as done in Löer et al. (2018). However, the artificial anisotropy introduced by the array geometry will be projected into the estimated results since the maximum beampower also depends on the orientation of station pairs determined by the array geometry. In this section, a modified CBF scheme is proposed to overcome the effect of the array geometry on the estimation of the azimuth-dependence phase velocity.

4.1. Algorithm for MCBF

As mentioned in section 3.1, due to the equivalence between SPAC in the frequency domain and NCFs in the time domain, NCFs can be thought as the sampling on the cylindrical wavefield described by $J_0(kr)$. We can do the following thought experiment. Assuming the array is dense enough and infinite, the Fourier transformed NCFs of each azimuth are arranged from $r=0$ to $r=\infty$ according to their interstation intervals. The spatial wavefield would be a cylindrical wave with $r=0$ as the center, as shown in Figure 5a. Note that the central point $r=0$ is a reference point and does not actually correspond to any physical position of the array.

The beamforming shown in Equation 7 is designed to track the phase by fitting the cylindrical wave shown in Figure 5a with the plane wave incident from different azimuth. As a function of θ, the beampower is thus obtained by summing over θ_{ij} which is implemented by projecting the plane wave into all the station-pairs. The averaged beampower over the azimuth θ is then used to estimate the azimuth-averaged velocity. The algorithm of WCBF shown in Equation 20 is the same as this process for Equation 7, but the geometric spread is corrected. The corrected cylindrical wavefield is shown in Figure 5b.

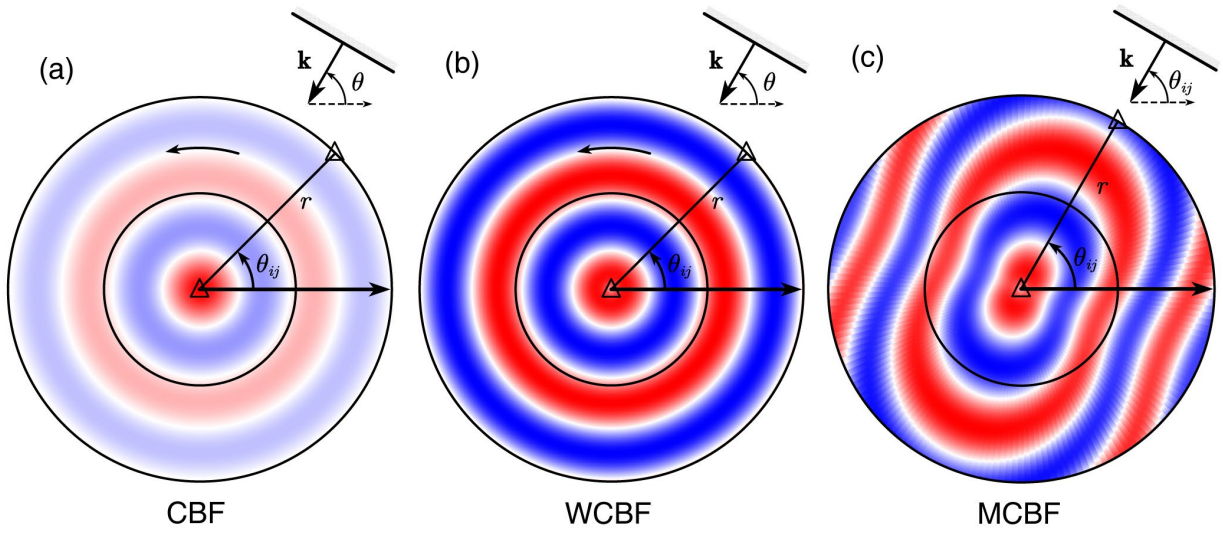

448

449 **Figure 5.** The schematic diagram of cylindrical wave field processed by different strategies of BF technique. (a)
450 The conventional CBF handle the cylindrical wavefield represented by $J_0(kr)$. The plane wave with a given
451 azimuth θ is projected into all the interstation pairs and the beamforming is output as a function of θ. (b) WCBF
452 handle the cylindrical wavefield with the correction factor $\sqrt{kr}$. The beamforming is also output as a function
453 of θ. (c) Only the plane waves with the same azimuth as the orientation θ_{ij} of the interstation pairs is
454 considered in MCBF. The beamforming is output as a function of θ_{ij}. The wavefield can therefore be azimuthally
455 anisotropic for MCBF.

456 The above algorithm for CBF and WCBF suffers from two deficiencies. First, more computations
457 are spent on projecting a plane wave at a given azimuth into the orientation of all station-pairs,
458 but the improvement of the dispersion image is trivial. Second and more importantly, the
459 implement of projection implies the structure beneath the array is azimuthally isotropic. As shown
460 in Figure 5c, for the wavefield with an azimuth-dependence velocity, the azimuthal anisotropy will
461 be an issue. The isotropic assumptions required by the projection algorithm in Equations 7 and 20
462 would fail. Although the azimuth-dependence velocity can be estimated by omitting the average
463 over the azimuth θ, the effect of the array geometry will be merged in the result due to the
464 projection algorithm. To this end, we modify Equation 20 by omitting the projection operation. For
465 the interstation with a given orientation, beamforming is conducted only for the plane wave

incident from the azimuth consistent with the interstation orientation. The modified beamforming can be expressed as

$$MCBF\left(k,\omega,\theta_{ij}\right)=\frac{1}{N^2}\sum_{i}^{N(\theta_{ij})}\sum_{j}^{N(\theta_{ij})}\sqrt{\pi kr_{ij}}C_{ij}\left(r_{ij},\omega\right)e^{\iota\left(kr_{ij}-\frac{\pi}{4}\right)} \tag{29}$$

We call Equation 29 the modified cross-correlation beamforming (MCBF). The $N(\theta_{ij})$ over the summation symbol means only the station pair with orientation θ_{ij} is taken, i.e., only the incident plane wave along the direction of the station-pair orientation is considered. Correspondingly, the vectors representing the wavenumber $\mathbf{k}$ and distance $\mathbf{r}_{ij}$ in Equation 20 degenerate into scalars in Equation 29. The vector dot product $\mathbf{k}\cdot\mathbf{r}_{ij}$ is replaced by the scalar product kr_{ij}. It must be pointed out that $-\pi/4$ phase shift is introduced in Equation 29 to balance the $-\pi/4$ phase shift appeared in CSDM caused by the stacking over noise sources in seismic interferometry. This $-\pi/4$ phase shift is absent in Equation 20 because the projection and summation over θ_{ij} would automatically introduce $-\pi/4$ phase shift, while the operation on the projection and summation is neglected in Equation 29.

Using the same procedure as that for CBF and WCBF, the azimuth-averaged phase velocity can be estimated by MCBF. Note that, the azimuth average of WCBF in Equation 21 is conducted over θ, the azimuth of the incident plane wave. For MCBF, the azimuth average is performed over θ_{ij}, the orientation of the station-pairs. This average is nothing but the summation of all station-pairs and thereby can be written as

$$\overline{MCBF}(k,\omega)=\frac{1}{N^2}\sum_{i}^{N}\sum_{j}^{N}\sqrt{\pi kr_{ij}}C_{ij}\left(r_{ij},\omega\right)e^{\iota\left(kr_{ij}-\frac{\pi}{4}\right)} \tag{30}$$

The imaging conditions can be written as

$$\begin{aligned} MCBF1&=\mathrm{Re}\left[\overline{MCBF}(k,\omega)\right]\\ MCBF2&=\mathrm{ABS}\left[\mathrm{Re}\left(\overline{MCBF}(k,\omega)\right)\right]\\ MCBF3&=\mathrm{ABS}\left[\overline{MCBF}(k,\omega)\right] \end{aligned} \tag{31}$$

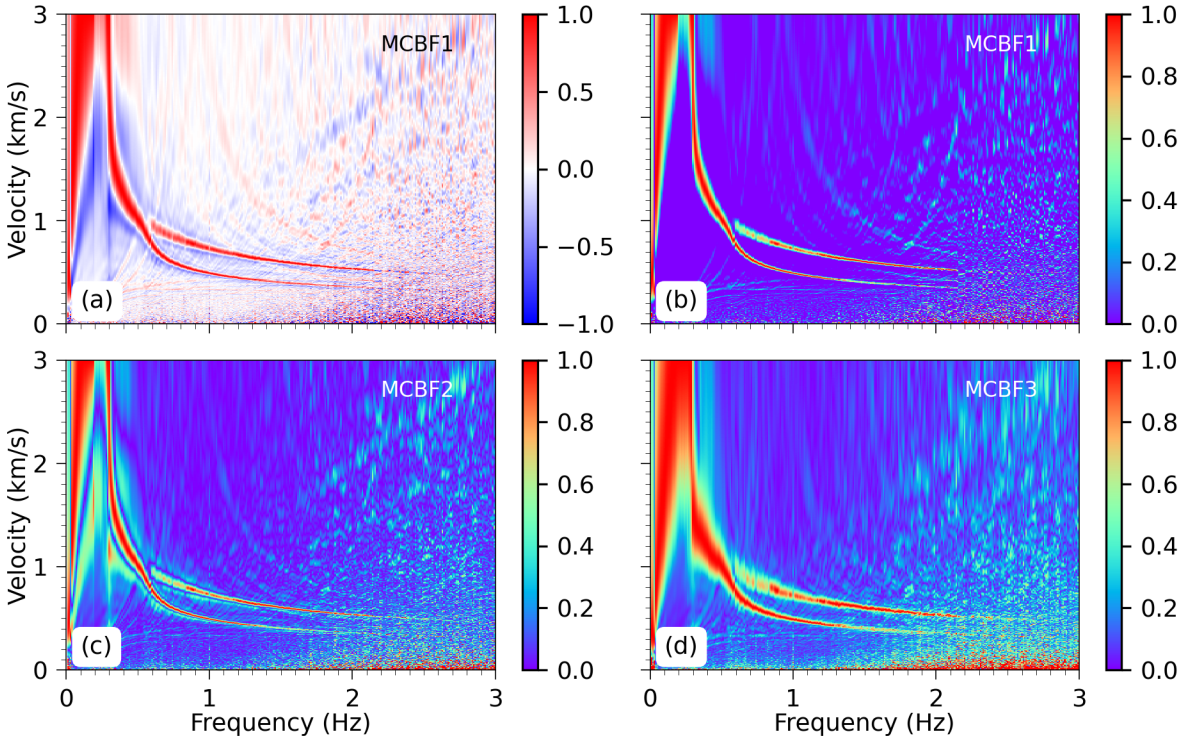

Figure 6. The dispersion images obtained by MCBF using the data from the array shown in Figure 1a. (a), (c) and (e) are the results for the imaging conditions shown in Equation 31. (b) is the same as (a) but only the positive value is color-coded.

Figure 6 shows the results obtained by MCBF using the data from the array shown in Figure 1a. Figure 6a shows the normalized result of MCBF1, the real part of the azimuth-averaged $\overline{MCBF}(k,\omega)$. The positive maxima are observed along two dispersion branches. The negative values, which are denoted by blue, appear adjacent to the maxima or spread in the image. These negative values originate from the product of the sinc and trigonometric functions (See Equation B13 in Appendix B for the theoretical representation of MCBF). If the absolute value of the real part of $\overline{MCBF}(k,\omega)$ is taken, i.e., the MCBF2 in Equation 31, side lobes would be observed on both side of the maxima, as shown in Figure 6c. These side lobes would disappear if the modulus of the of $\overline{MCBF}(k,\omega)$ is taken as the imaging condition, but the width of the main lobe would broaden as expected, as shown in Figure 6d. Therefore, a suitable display for the dispersion image is to color-code only the positive values of the real part of $\overline{MCBF}(k,\omega)$, as shown in Figure 6b. This display makes the dispersion image look clearer and easier to identify especially for the case

503 that the velocity of the modes is approaching.

504 Moreover, the assumption on the laterally isotropy is not required in MCBF. For the case of
505 azimuthal anisotropy, the azimuth-dependence velocity can be extracted using MCBF by
506 processing the beamforming output at each azimuth θ_{ij}, which is exactly the azimuth of the
507 incident plane wave. Different from the estimation of azimuth-dependence velocity using CBF or
508 WCBF, the spurious azimuthal anisotropy introduced by the array geometry would not be merged
509 into the results of MCBF since the projection to the orientation of the station pair in CBF or WCBF
510 is omitted in MCBF. The correction on the azimuth anisotropy introduced by array geometry, as
511 done in Lu et al. (2018), is not required.

512 **4.2. The Other Imaging Conditions**

513 Theoretically, the cross spectra $C_{ij}(r_{ij},\omega)$ of the vertical component in Equation 30 is real and
514 equivalent to the Bessel function $J_0(kr)$ if the noise field is perfectly isotropic. However, it is
515 usually complex in practice due to the complicated source feature. Different from Equation 30, we
516 can use the real part of $C_{ij}(r_{ij},\omega)$ to approximate $J_0(kr)$. At the same time, instead of the complex
517 exponential function, the sine or cosine functions are used to present the plane wave. The
518 corresponding imaging conditions can be expressed as

519
$$MCBF4(k,\omega)=\frac{1}{N^2}\sum_{i}^{N}\sum_{j}^{N}\sqrt{kr_{ij}}\,\mathrm{Re}\left[C_{ij}\left(r_{ij},\omega\right)\right]\cos\left(kr_{ij}-\frac{\pi}{4}\right)$$
$$MCBF5(k,\omega)=\frac{1}{N^2}\sum_{i}^{N}\sum_{j}^{N}\sqrt{kr_{ij}}\,\mathrm{Re}\left[C_{ij}\left(r_{ij},\omega\right)\right]\sin\left(kr_{ij}-\frac{\pi}{4}\right) \quad (32)$$

520 It is assumed that the cylindrical wavefield described by $J_0(kr)$ contains two surface wave
521 eigenvalues $k_1=1$ and $k_2=10$. We investigate the effect of different imaging conditions on the
522 result by comparing the beamforming output of such an ideal cylindrical wavefield. The results are
523 given in Figure 7. In simulation, the spatial wavefield is uniformly sampled with $\Delta r=0.2$ and the
524 maximum distance $r_{\max}=6.0$. The wavenumber and distance are dimensionless.

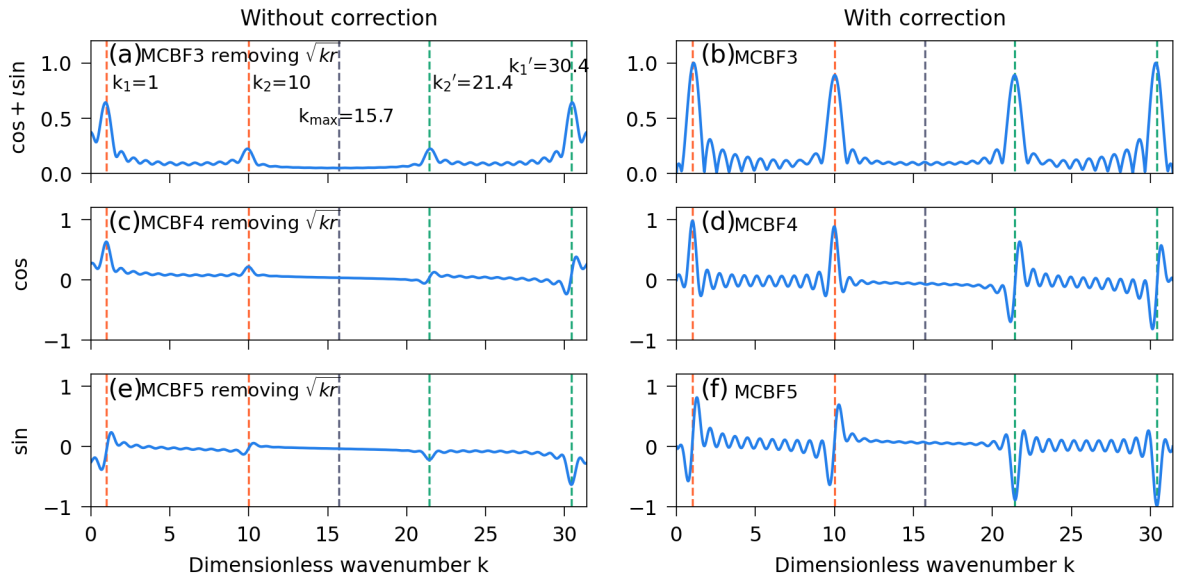

525

526 **Figure 7**. The beamforming output by applying MCBF with different basis functions to a cylindrical wavefield
527 containing two eigen-wavenumbers (k=1 and k=10). (b) The result of MCBF3, where the complex exponential
528 function is taken as the basis function. (d) and (f) are the results of MCBF4 and MCBF5, where the cosine and
529 sine functions are taken as the basis function, respectively. (a), (c) and (e) show the corresponding results by
530 removing the term $\sqrt{kr}$ in Equations 30 and 32.

531 In Figure 7, right panels show the results of MCBF3, MCBF4 and MCBF5. The left panels show the
532 corresponding results without the correction for geometric spread, i.e., the results of MCBF3,
533 MCBF4 and MCBF5 but removing the correction term $\sqrt{kr}$. The vertical red dashed line denotes
534 the location of the eigen-wavenumbers. The vertical gray dashed line denotes the location of
535 resolving maximum wavenumber $k_{\max} = \pi/\Delta r = 15.7$ estimated by Equation 15. Aliasing occurs at
536 the wavenumbers greater than $k_{\max}$ ($k > k_{\max}$). The aliasing wavenumbers are
537 $k_1^{'} = 2k_{\max} - k_1 = 30.4$ and $k_2^{'} = 2k_{\max} - k_2 = 21.4$, which are denoted by vertical green dashed lines.

538 It can be found from Figure 7: 1) The result of MCBF5 is the antisymmetry of that of MCBF4, as
539 shown in Figures 7d and 7f. The target wavenumbers k_1 and k_2 are associated with the maxima
540 of the beamforming output if cosine function is selected as the basis, while they are associated
541 with the zero-crossing points for sine basis function. On the contrary, the aliasing wavenumbers
542 $k_1^{'}$ and $k_2^{'}$ are associated with the (negative) maxima for sine basis function, while they are

associated with the zero-crossing points for cosine basis function. If the modulus is taken as the imaging conditions, the zero-crossing points associated with the target (or aliasing) wavenumbers would behave as a trough between two extremes (See Figure S1 in the supporting information where the modulus of MCBF4 and MCBF5 is plotted). 2) Compared with the results of MCBF4 based on the cosine function, the results of MCBF3 based on the exponential function have a wider main lobe but fewer side lobes. This is more evident if the modulus of MCBF4 is taken (See Figure S1 in the suporting information). 3) Both the traget wavenumbers k_1, k_2 and the aliasing wavenumbers $k_1^{'}, k_2^{'}$ are associated with the maximum for the result of MCBF3. 4) The actual amplitudes, which are supposed to be 1 for two eigen-wavenumbers, can not be recovered without the correction term $\sqrt{kr}$. This results in a dispersion image that lacks clarity at high frequencies, as shown in Figure 1b.

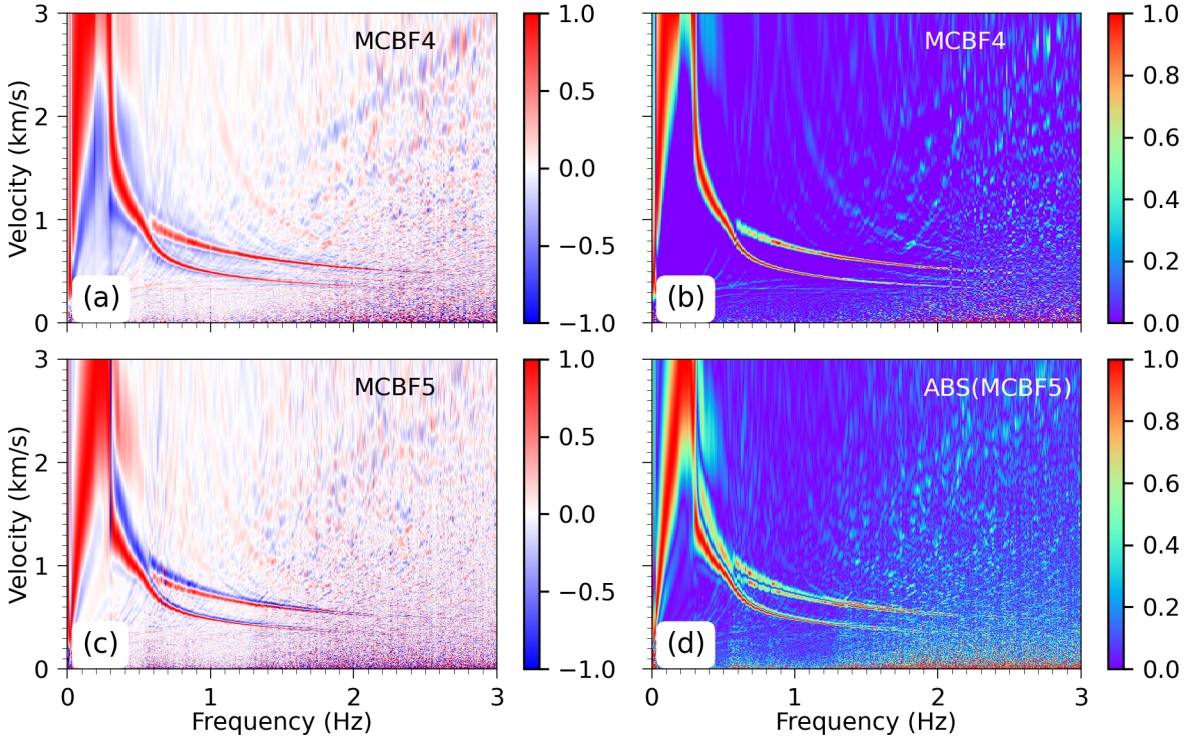

Figure 8. The dispersion images obtained by MCBF (Equation 32) using the data from the array shown in Figure 1a. (b) is the same as (a) but only the positive value is color-coded.

Figure 8 shows the results obtained by MCBF4 and MCBF5 using the data from the array shown in Figure 1a. As discussed above, the eigenvalues along the dispersion branches corresponds to the

maxima for the results of MCBF4. For the results of MCBF5 based on sine function, the eigenvalues along the dispersion branches corresponds to the zero-crossing points. Since there are many zero points spread in the image, it brings the handicap for the picking of the eigenvalues along dispersion branches. Color-coding only the positive value of MCBF4 is proved to be a better imaging condition, as shown in Figure 8b, where the dispersion image has a high resolution without side lobes such as occurred in Figure 8a, 8c and 8d. Furthermore, the result of MCBF4 is almost the same as those of MCBF1 shown in Figure 6. This means the distribution of the noise source is fairly uniform and hence the SPAC coefficient is supposed to be close to $J_0(kr)$ with a negligible imaginary part.

4.3. Relation Between MCBF and F-J Method

In practice, the sampling on the wavefield in space is always finite and usually non-uniform due to the finite NCFs and irregular array. The integral over the distance r in Equation 25 from 0 to infinite is often replaced by a finite interval. Since the relative rather than the absolute magnitude of the spectrum in f-v domain is of interested, the integral is therefore normalized by the integral length. We have

$$FJ(k,\omega) = \frac{1}{R}\int_0^R C_{ij}(r,\omega)J_0(kr)rdr \tag{33}$$

For an array with N stations, the number of the station-pairs is $M = N(N-1)/2$. The interstation distances are arranged in order from smallest to largest as $r_1, r_2, \cdots, r_j, \cdots, r_M$. The integral of Equation 33 can be approximated numerically by

$$\begin{aligned} FJ(k,\omega) = &\frac{1}{r_2 - r_1}\int_{r_1}^{r_2} C(r)J_0(kr)rdr + \cdots \\ &+ \frac{1}{r_{j+1} - r_j}\int_{r_j}^{r_{j+1}} C(r)J_0(kr)rdr + \cdots \\ &+ \frac{1}{r_M - r_M}\int_{r_{M-1}}^{r_M} C(r)J_0(kr)rdr \end{aligned} \tag{34}$$

Using the trapezoidal integral formula

$$\int_a^b f(x)dx = (b-a)\frac{f(a)+f(b)}{2} \tag{35}$$

Equation 34 can then be expressed as

$$FJ(k,\omega) \approx \frac{1}{2}C(r_1)J_0(kr_1)r_1 + \sum_{j=2}^{M-1} C(r_j)J_0(kr_j)r_j + \frac{1}{2}C(r_M)J_0(kr_M)r_M$$

581
$$\approx \sum_{j=1}^{M} C(r_j)J_0(kr_j)r_j \approx \sum_{j=1}^{M} C(r_j)r_j\sqrt{\frac{2}{\pi kr_j}}\cos(kr_j - \frac{\pi}{4}) \quad (36)$$

$$\approx \sqrt{\frac{2}{\pi k}}\sum_{j=1}^{M} C(r_j)\sqrt{r_j}\cos(kr_j - \frac{\pi}{4})$$

582 The far approximation of $J_0(kr)$ shown in Equation 19 are applied in Equation 36.

583 On the other hand, the azimuth-averaged MCBF shown in Equation 30 can be recast into

584
$$\overline{MCBF}(k,r) = \frac{1}{N^2}\sum_{i}^{N}\sum_{j}^{N}\sqrt{\pi kr_{ij}}C_{ij}(r_{ij},\omega)e^{\iota\left(kr_{ij}-\frac{\pi}{4}\right)} = \frac{\sqrt{2}\pi k}{N^2}\left(\frac{\sqrt{2}}{\sqrt{\pi k}}\sum_{j=1}^{M} C(r_j)\sqrt{r_j}e^{\iota\left(kr_j-\frac{\pi}{4}\right)}\right) \quad (37)$$

585

586 In practical applications, the real part of $C(r_{ij})$ is usually taken in F-J method. Ignoring the
587 difference caused by tiny imaginary part and comparing Equations 36 and 37, it can be found that
588 the relationship between MCBF and F-J is

589
$$\mathrm{Re}\left[\overline{MCBF}(k,\omega)\right] \approx MCBF4 = \frac{\sqrt{2}\pi k}{N^2}FJ(k,\omega) \quad (38)$$

590 That is to say, as far as the measurement of the azimuth-averaged phase velocity, MCBF is also
591 equivalent to F-J, differing by a factor of $1/k$. If we dividing MCBF4 by k to remove the correction
592 on the wavenumber in Figure 8b, the disturbing pixels around the area near the zero velocity would
593 be reduced and the resulted dispersion image would comparable to those shown in Figure 4c and
594 4e, the results of WCBF3 and F-J. Although it is the cosine rather than Bessel function appears in
595 MCBF, the correction on the wavenumber in MCBF reduces the near field effect. The extracted
596 velocity values are quite consistent with that given by WCBF and F-J, even at low frequencies, as
597 shown in Figure 4f.

598 As discussed before, similar as the extraction of azimuth-averaged velocity by CBF and WCBF, the
599 velocity obtained by F-J is also the azimuth-averaged. Although F-J and MCBF are also equivalent
600 for the estimation on azimuth-averaged velocity, the azimuth-dependence velocity can be
601 estimated using MCBF by picking the velocities associated with the maxima of the beampower at
602 a given azimuth. This cannot be achieved in principle via F-J by considering only the NCFs at a given
603 azimuth. This is because the Bessel function appears in the F-J integration is the result of integrating

the exponential function over the omnidirectional azimuth. If only the NCFs at a given azimuth are considered in F-J, the Bessel function should be replaced by the exponential function, i.e., the MCBF scheme.

5. Aliasing and Its Reduction

The aliasing is inevitable in practical applications due to the finite sampling. In this section, we demonstrate the aliasing features in terms of a simple cylindrical wavefield containing three eigen-wavenumbers. Based on the theoretical representation of MCBF for the array with finite stations, a scheme is then proposed to eliminate the aliasing introduced by negative wavenumber.

5.1. Aliasing and Its Features

The CSDM of a cylindrical wavefield containing three dimensionless eigen-wavenumbers $k_1 = 1$, $k_2 = 10$ and $k_3 = 25$ can be expressed as $C(r,\omega) = J_0(k_1 r) + J_0(k_2 r) + J_0(k_3 r)$. For the same sampling as that used in Figure 7, i.e., $\Delta r = 0.2$ and $r_{\max} = 6.0$, the resolved maximum and minimum wavenumber are respectively $k_{\max} = \pi / r_{\min} = 15.7$ and $k_{\min} = \pi / r_{\max} = 0.52$.

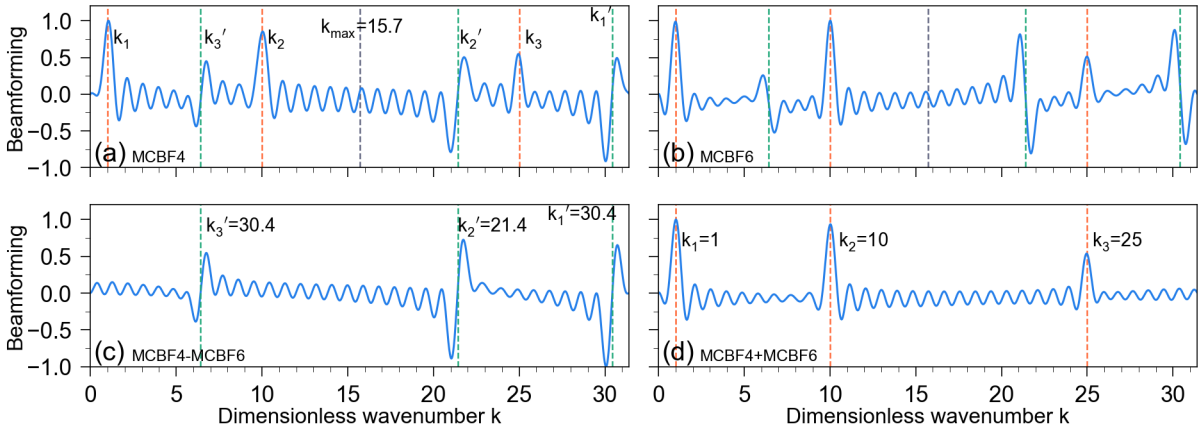

Figure 9. An illustration for aliasing wavenumbers and its reduction. The results are calculated by different imaging conditions for a cylindrical wavefield containing three eigenvalues of horizontal wavenumbers $k_1 = 1$, $k_2 = 10$ and $k_3 = 25$, which are denoted by vertical red dashed lines. The corresponding aliasing wavenumbers $k_1^{'}$, $k_2^{'}$ and $k_3^{'}$ are denoted by vertical green dashed lines. The resolved maximum wavenumber is denoted by gray dashed line. (a) The result of MCBF4. (b) The result of MCBF6. (d) The result of MCBF4-MCBF6. (d) The result of MCBF4+MCBF6.

Figure 9a shows the beamforming output of MCBF4. Three target eigen-wavenumbers are denoted by vertical red dashed lines. $k_{\max}$ estimated by Equation 15 is denoted by gray dashed line. Two aliasing wavenumbers $k_1^{'} = 2k_{\max} - k_1 = 30.4$ and $k_2^{'} = 2k_{\max} - k_2 = 21.4$ caused by the symmetry of k_1 and k_2 are observed at $k > k_{\max}$, as shown by the vertical green lines. Similarly, due to the symmetry of k_3, aliasing wavenumber $k_3^{'} = 2k_{\max} - k_3 = 6.4$ is observed at $k < k_{\max}$. The target wavenumbers correspond to the positive peaks of the beamforming output, while the aliasing wavenumbers are related to the zero-crossing points between two positive and negative peaks. If the modulus is taken as the imaging condition, the aliasing wavenumbers would behave as a trough between two extremes (See Figure S2 in the supporting information where the modulus is taken as the value for plotting). The presence of $k_3^{'}$ could affect the identification of the eigen-wavenumbers k_1 and k_2, even if only the resolved target wavenumbers range $[k_{\min}, k_{\max}]$ determined by the sampling theorem is considered.

5.2. Theoretical Representation for Aliasing and Its Reduction

Aliasing arises from the sampling on the traveling waves at two directions (Forbriger, 2003). The spatial wavefield described by $J_0(kr)$ can be thought as a cylindrical standing wave, which is the superposition of two cylindrical traveling waves propagating inward and outward. The $J_0(k_n r)$ can be expressed as

$$J_0\left(k_n r\right) = 1/2\left[H_0^{(1)}\left(k_n r\right) + H_0^{(2)}\left(k_n r\right)\right] \tag{39}$$

where $H_0^{(1)}$ and $H_0^{(2)}$ are respectively the first and second kind of Hankel function with zero-order. According to the convention of Fourier transform given in Appendix A, $H_0^{(1)}$ represents the cylindrical wave propagating inwards while $H_0^{(2)}$ represents the cylindrical wave propagating outwards. For the imaging condition MCBF4 in Equation 32, a plane wave represented by cosine function is used to fit the cylindrical standing wave via the operation of delay-and-sum. This means that two cylindrical waves propagating in opposite directions are fitted simultaneously. The eigen-wavenumbers could be also estimated for the propagating wave inwards, i.e., propagating along direction $-\mathbf{k}$. In the range $[0, 2k_{\max}]$, the aliasing wavenumber $k_n^{'}$ can be observed at

650 $k_n^{'} = 2k_{\max} - k_n$ due to the symmetry with the target wavenumber for $+\mathbf{k}$ direction.

651 Similar to the discussion in Xi et al. (2021) and Zhou and Chen (2021), we define MCBF6 as

652 $$MCBF6(k,\omega) = \frac{1}{N^2}\sum_i^N\sum_j^N \sqrt{\pi r_{ij} k}\left\{\mathcal{H}\left(\mathrm{Re}\left[C_{ij}\left(r_{ij},\omega\right)\right]\right)\sin\left(kr_{ij} - \frac{\pi}{4}\right)\right\} \quad (40)$$

653 The symbol $\mathcal{H}$ represents the Hilbert transform, the convention of which is given in appendix A.
654 For the ideal cylindrical wavefield, $C(r,\omega) = J_0(k_n r)$, and its Hilbert transform is $Y_0(k_n r)$, the zero
655 order Bessel function of the second kind. Figure 9b shows the output of MCBF6, where both the
656 actual and aliasing wavenumbers are observed. For the beampower around the positive peaks
657 associated with the target wavenumbers, the result of MCBF6 is the same as that of MCBF4.
658 However, for the beampower around the zero-crossing points associated with aliasing
659 wavenumbers, the result of MCBF6 is the Centro symmetry of MCBF4. This means that the aliasing
660 wavenumbers can be removed by summing the results of MCBF4 and MCBF6. In fact, the
661 elimination of aliasing wavenumbers can be demonstrated analytically by investigating the
662 theoretical representations of MCBF4 and MCBF6 for the finite sampling.

663 Substituting $C(r,\omega) = J_0(k_n r)$ into Equations 32 and 40, for the sampling with small equal interval
664 Δr, we have (See appendix B for details)

665 $$\begin{aligned} MCBF4 &= \frac{\sqrt{2}M}{N^2}\frac{\sqrt{k}}{\sqrt{k_n}}\left[\cos\frac{R(k_n-k)}{2}\,\mathrm{sinc}\frac{R(k_n-k)}{2} + \sin\frac{R(k_n+k)}{2}\,\mathrm{sinc}\frac{R(k_n+k)}{2}\right] \\ MCBF6 &= \frac{\sqrt{2}M}{N^2}\frac{\sqrt{k}}{\sqrt{k_n}}\left[\cos\frac{R(k_n-k)}{2}\,\mathrm{sinc}\frac{R(k_n-k)}{2} - \sin\frac{R(k_n+k)}{2}\,\mathrm{sinc}\frac{R(k_n+k)}{2}\right] \end{aligned} \quad (41)$$

666 where $\mathrm{sinc}(x) = \sin x/x$ is the sinc function, and $M = N(N-1)/2$. It can be found from Equation
667 41 that the terms containing $k_n - k$ and $k_n + k$ are linearly separated. The linear combinations of
668 MCBF4 and MCBF6 can be used to separate the terms containing only the argument $k_n - k$ from
669 the terms containing only argument $k_n + k$. The corresponding imaging conditions can be
670 expressed as

$$MCBF4+MCBF6=\frac{2\sqrt{2}M}{N^2}\frac{\sqrt{k}}{\sqrt{k_n}}\cos\frac{R(k_n-k)}{2}\operatorname{sinc}\frac{R(k_n-k)}{2}$$
$$MCBF4-MCBF6=\frac{2\sqrt{2}M}{N^2}\frac{\sqrt{k}}{\sqrt{k_n}}\sin\frac{R(k_n+k)}{2}\operatorname{sinc}\frac{R(k_n+k)}{2} \quad (42)$$

Figure 9c shows the result of $MCBF4-MCBF6$. Only the aliasing wavenumbers are observed at the zero-crossing points which are associated with $k_n^{'}=2k_{\max}-k_n\ (n=1,2,3)$. Figure 9d shows the result of $MCBF4+MCBF6$ where only the actual wavenumbers propagating in $\mathbf{k}$ direction are kept, which are associated with the positive peaks at $k=k_n$. Therefore, the linear combination $MCBF4+MCBF6$ can be used to remove the aliasing caused by the propagating wave in $-\mathbf{k}$ direction.

5.3. Numerical Simulation and the Example of the Field Data

Table 1. The layered model (Zhou and Chen, 2021)

Layer thickness (km)	P wave velocity (km/s)	S wave velocity (km/s)	Density (g/cm^3)
0.025	1.35	0.2	1.9
∞	2.0	1	2.5

In this section, the aliasing and its reduction are investigated by numerical simulation. The two-layered model shown in Table 1 is considered. This model has been discussed in Wathelet et al. (2008), Xi et al. (2021) and Zhou and Chen (2021). The quality factor Q is neglected here since it does not affect current discussion. The vertical component of Rayleigh wave is considered in the numerical simulation. Substituting the CSDM represented by Equation 18 into Equations 32 and 40, the dispersion images in f-v and f-k domain can be obtained by the imaging conditions MCBF4 and MCBF6 and their linear combinations.

In the simulation, we take the maximum radial distance $r_{\max}=200m$ and the interval $\Delta r=10m$. Figure 10 shows the final results for different imaging conditions. Figure 10a and 10e show the results of MCBF4 in f-k and f-v domain, respectively. The corresponding results of MCBF6 are

presented in Figure 10b and 10f. The aliasing wavenumbers caused by the waves propagating in $-\mathbf{k}$ direction can be observed in Figure 10a and 10b, which appears as the maxima energy belt with negative slope. In f-v domain, as shown by Figure 10e and 10f, this aliasing appears as a hyperbolic shape with vertex close to the origin. As expected, the sign of the result on either side of the zero-crossing points associated with the aliasing wavenumber is reversed for MCBF4 and MCBF6. The target wavenumbers are associated with the maxima both for MCBF4 and MCBF6. As a result, this aliasing can be separated and removed using the linear combinations of MCBF4 and MCBF6. The separated aliasing in f-k and f-v domain are respectively shown in Figure 10d and 10h, which are the results of $MCBF4-MCBF6$. Figure 10c and 10g show the corresponding results of $MCBF4+MCBF6$, where the aliasing caused by waves propagating in $-\mathbf{k}$ direction is removed.

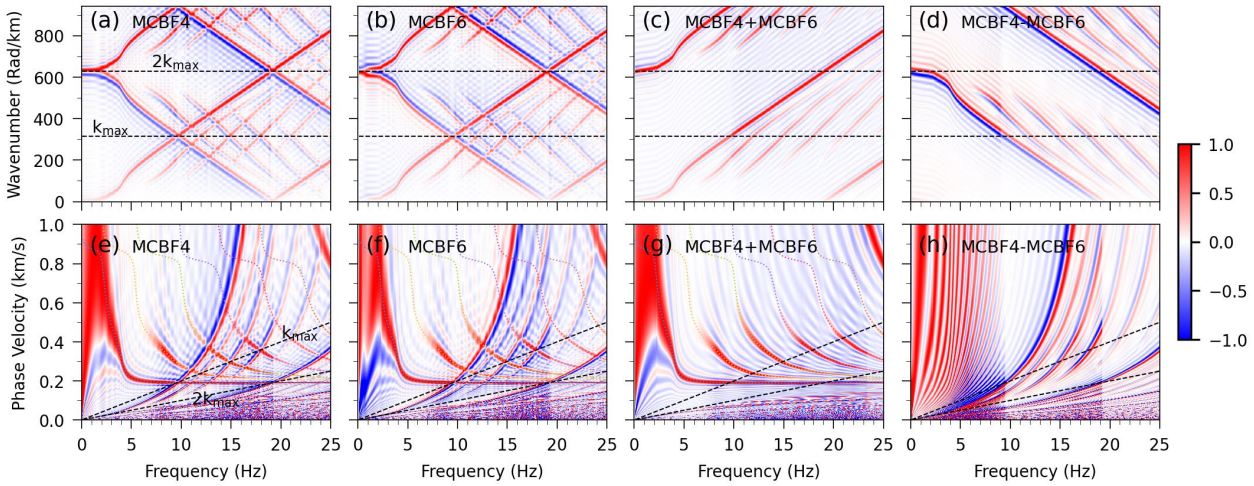

Figure 10. An illustration of the aliasing and its reduction. The panels at top row are the results in f-k domain while the panels at lower row are the corresponding results in f-v domain. (a) The dispersion image in f-k domain obtained MCBF4. (b) The result of MCBF6. (c)The result of MCBF4+MCBF6. The aliasing caused by the waves propagating in $-\mathbf{k}$ direction is removed. (d)The separated aliasing obtained by MCBF4-MCBF6. (e)-(h) are the corresponding results in f-v domain of (a)-(d). The wavenumber of $k_{\max}$ and $2k_{\max}$ are denoted by black dashed lines.

In Figure 10a, there also exist another periodic aliasing caused by limited sampling. Opposite to the aliasing shown in Figure 10d, the energy belts presented this periodic aliasing has a positive slope in f-k domain, as shown in the area above the dashed line of $k=2k_{\max}$ in Figure 10c. This periodic aliasing repeats with a period of $2k_{\max}$ and cannot be removed using $MCBF4+MCBF6$. As an

artifact, this periodic aliasing appears more pronounced in f-k domain. In f-v domain, as shown in Figure 10g, it appears in the area under the black dashed line of $k = 2k_{\max}$, a region with high frequency but low velocity. Therefore, in the resolved frequency range determined by sampling, this aliasing generally has little impact on the identification of dispersion curves in f-v domain.

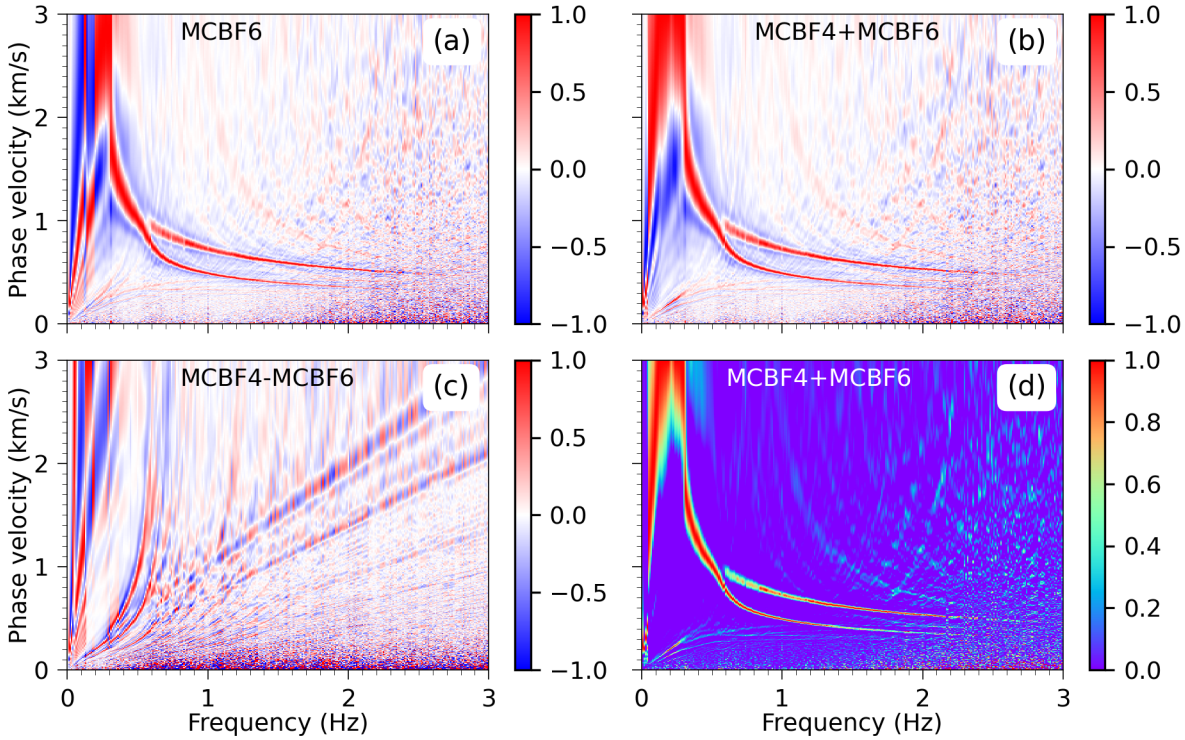

Figure 11. An illustration for the separation and elimination of the aliasing wavenumbers for the array shown in Figure 1a. (a) The result of MCBF6. (b) The result of MCBF4+MCBF6. (c) The result of MCBF4-MCBF6. (d) The same as (b) but only the positive values are color-coded.

Figure 11 presents the results of MCBF6 and the linear combination of MCBF4 and MCBF6 for the data from the array shown in Figure 1a. It shows the improvement of the dispersion image after removing aliasing by the imaging conditions MCBF4+MCBF6 is not significant. In other words, the aliasing of the dispersion image given by MCBF4 itself is not obvious, as shown in Figure 8b. We speculate that this is related to the irregular station distribution of the real array. The summation over the NCFs inside the array reduces the aliasing. This is different from the numerical simulation shown in Figure 10e, where the regular sampling with equal intervals is adopted. The fact that the

aliasing can be reduced by random station distribution can also be observed for the synthetic data in section 6.1.

6. Synthetic Data and More Examples of the Real World

6.1. Example of the Synthetic Data

6.1.1. Model and the Synthesis of Ambient Seismic Noise

In this section, we investigate the extraction of multimode dispersion curves of Rayleigh wave using WCBF and MCBF based on the synthetic data. The same layered model shown in Table 1 is considered.

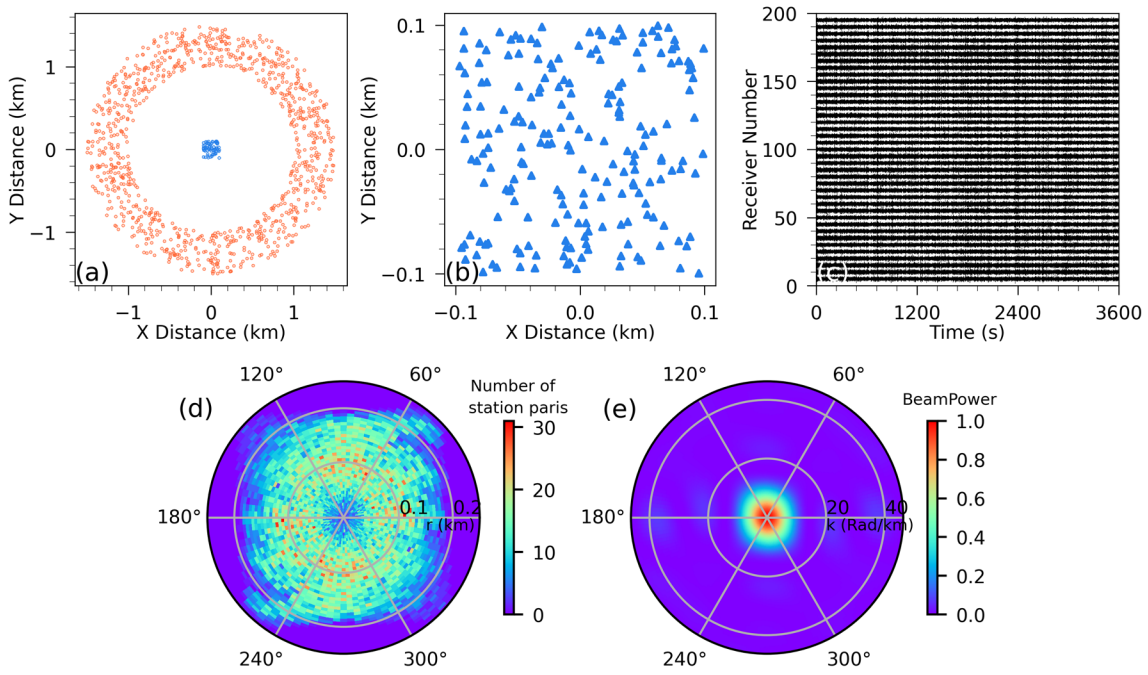

Figure 12. (a) The source (red dots) distribution and the receiver (blue triangles) array. (b) The random distributed stations of the receiver array. (c) Examples on the segments of synthetic ambient noise recording. (d) The distribution of the number of station pairs as a function of the interstation distance and azimuth. (e) The ARF of the receiver array.

To synthesize the data, 10,000 sources randomly distributed over 1.0-1.5 km annular region are used to excite the vertical component of the Rayleigh wave, as shown by the red dots in Figure 12a. Each source is assumed to be the vertical point force with random intensity between 0-1. The source function is a Ricker wavelet with center frequencies distributed randomly between 0-25 Hz.

744 The onset time of the sources is distributed randomly between 0-3,600 s. The waveform at the
745 receiver excited by each source is calculated by the dot product of the vertical point force and the
746 Green's function shown in Equation 18. The noise data with 1-hour duration is then synthesized by
747 summing the waveform for all sources. As shown in Figure 12a and 12b, 200 stations distributed
748 randomly within a square array of 0.2 km × 0.2 km are designed to record the noise data. Figure
749 12c shows some segments of the synthetic ambient noise recording at 40 stations. Figure 12d
750 shows the distribution of the number of station pairs as a function of the interstation distance and
751 azimuth. Figure 12e shows the ARF of the array.

752 **6.1.2. Wavefield and Multimode Dispersion Curves Extracted by WCBF and MCBF**

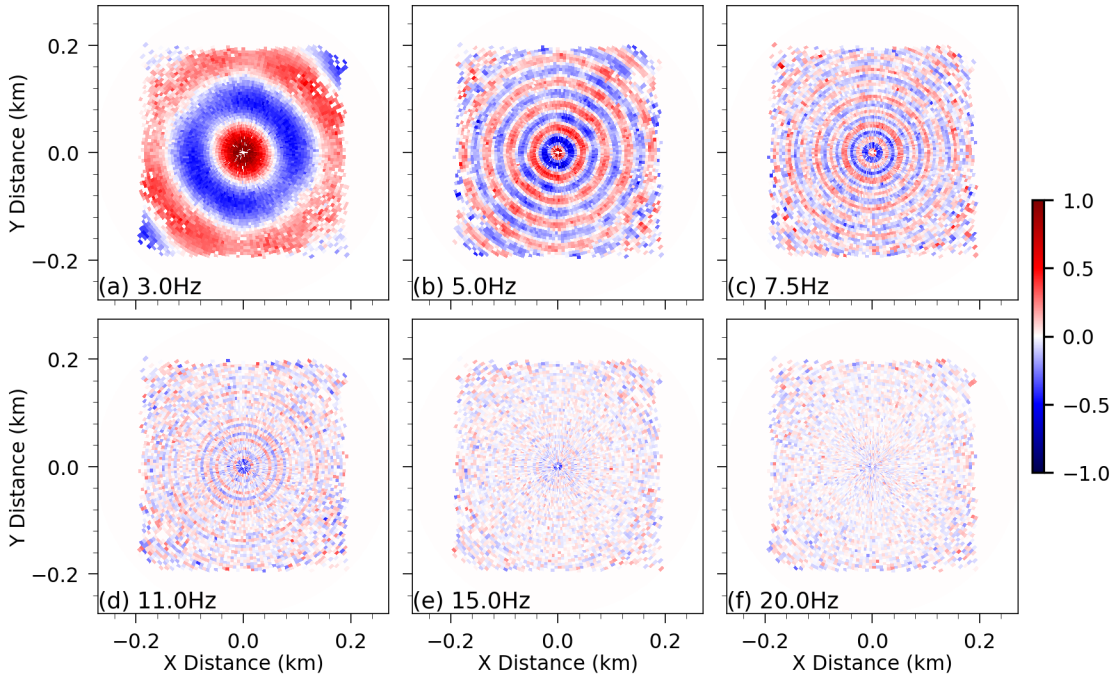

753

754 **Figure 13.** The wavefield (real part of the Fourier transformed NCFs) at six selected frequencies across the array
755 shown in Figure 12b, plotted as a function of the orientation (azimuth) and interstation distance (radial direction).
756 The amplitude in each panel is normalized by the maximum.

757 Plotted as a function of the orientation and interstation distance, the wavefield at six selected
758 frequencies across the array shown in Figure 12b are presented in Figure 13. They are the real part
759 of the Fourier transformed NCFs of the interstation inside the array. The amplitude in each panel is
760 normalized by the maximum.

As we discussed in sections 3.2 and 4.3, under the assumption of lateral isotropy, if the distribution of the sources and the interstation orientation is uniform enough, the wavefield would be radially symmetric. The wavefield at different azimuth can be projected into the radial direction, as shown in Figure 14. The spectrum of NCFs is then just a radial sampling on the cylindrical wavefield across the array by arranging the NCFs according to their interstation distance. For F-J method, the integral over the distance r is conducted using the sampling values shown in Figure 14. This operation is similar as the azimuth-average in BF.

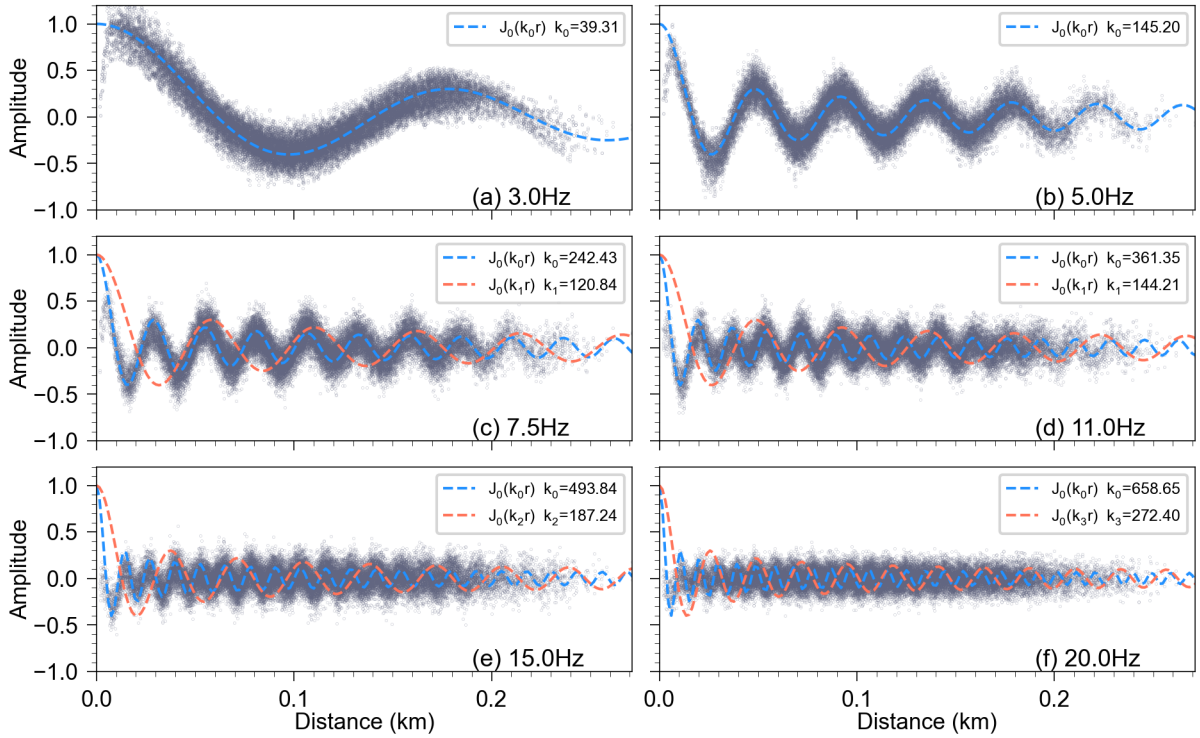

Figure 14. The wavefield variation as a function of radial distance by projecting results at six frequencies in Figure 13 into one direction. The blue and red dashed lines represent the Bessel functions $J_0(kr)$ with argument kr.

In Figure 14, the blue and red dashed lines represent the Bessel functions $J_0(kr)$ with argument kr. The wavenumber k associated with the eigenvalues are labeled with corresponding color. It can be found the variation of the wavefield can be approximated by $J_0(kr)$ if only one eigen-wavenumber is expected, as illustrated by Figures 14a and 14b where only one mode is observed at frequencies 3 and 5 Hz. If more than one eigen-wavenumbers are expected, the wavefield will

776 be the weighted superposition such as $\sum_n W_n J_0(k_n r)$ as shown in Figure 14c-14f where more
777 than one mode is observed at frequencies 7.5, 11, 15 and 20 Hz. It seems that the Bessel function
778 $J_0(k_0 r)$ with characteristic wavenumber k_0 of the fundamental mode fit well with the synthetic
779 wavefield in Figure 14c-14f. This is because the fundamental mode makes a major contribution to
780 the synthetic record (See Figure S3 in the supporting information for the fit of the theoretical and
781 synthetic wavefield at frequencies 7.5, 11, 15 and 20 Hz).

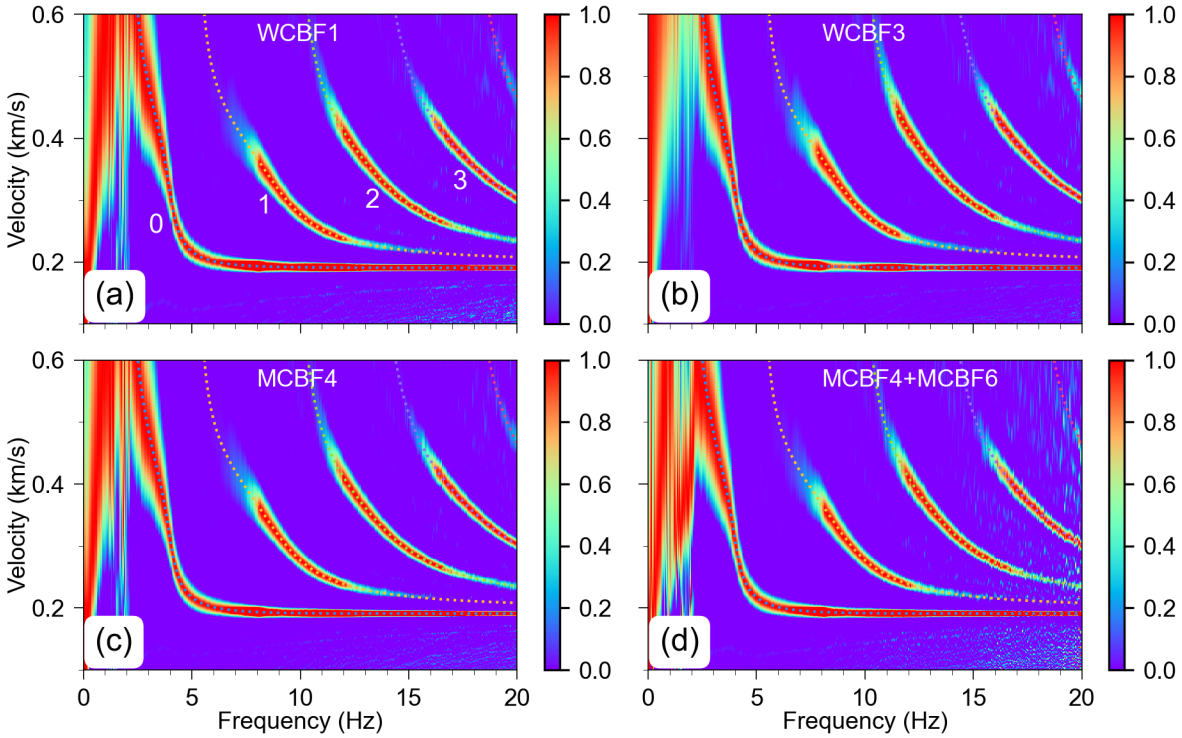

782

783 **Figure 15.** The dispersion image obtained by different beamforming schemes. (a) The result of WCBF1. (b) The
784 result of WCBF3. (c) The result of MCBF4. (d) The result of MCBF4+MCBF6.

785 Figure 15 shows the dispersion images obtained by different beamforming schemes. The dispersion
786 curves of the first four modes (modes 0-3) can be observed clearly from the results of WCBF and
787 MCBF. The difference between WCBF and MCBF is slight since the model is lateral isotropic. As we
788 observed in Figure 8b for the data from the field data, significant aliasing is not observed in the
789 result of MCBF4 in Figure 15c. Even the tiny interferences can be observed at frequencies higher
790 than 15 Hz for the result by antialiasing strategy MCBF4+MCBF6, as shown in Figure 15d. As

discussed before, we attribute this to the random distribution of stations in the array. Unlike the regular sampling, aliasing is not coherent for random sampling. As a result, the aliasing is reduced even for the result of MCBF4 for the array with station distributed randomly. As a verification, in Figure S4 of the supporting information, we present an example of the synthetic data for the array with stations regularly distributed. We find that for the array with stations regularly distributed, the manifest aliasing appears for the results of MCBF4, while antialiasing strategy MCBF4+MCBF6 can effectively eliminate the aliasing (See Figure S4 in the supporting information).

6.2. More Examples at Different Scales

6.2.1. Example for a Nearly Linear Array in Haiyuan

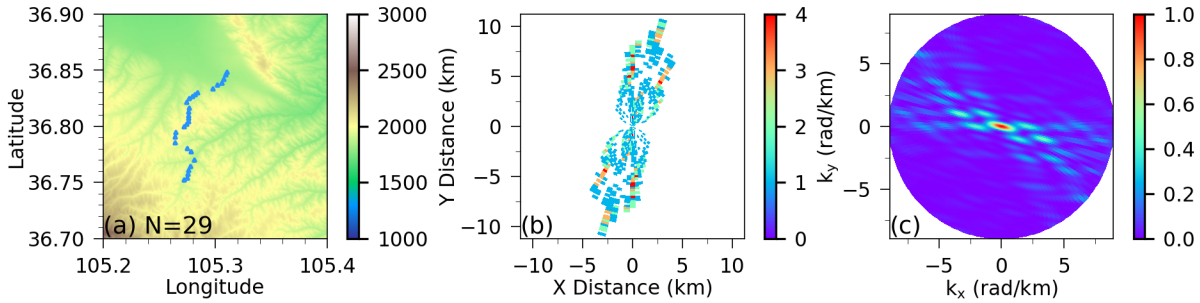

Figure 16. (a) The station distribution of the subset (twenty-nine stations) from Haiyuan array. (b) The distribution of the number of station pairs as a function of interstation spacing and azimuth. (c) The ARF of the array in (a).

The extraction of multimode Rayleigh waves using WCBF and MCBF are illustrated above based on the data from Tongzhou array which is located in the east of Beijing, and mainly on the north China plain (Qin et al, 2022). An example using the data from the other array located on the northwest China is investigated in this section. The array consists of more than 600 stations with a spacing of 300m–2km, and observations were conducted around the Haiyuan fault from October 2020 to December 2020. The Haiyuan fault is a main active fault in northwest China, and the 1920 M8.0 earthquake occurred on this fault. The array is designed to investigate the fine structure around the fault. The subset stations in the array as shown in Figure 16a were chosen to illustrate the extraction of multimode surface waves by WCBF and MCBF. The stations of this subarray are roughly linearly distributed. The minimum and maximum interstation distance are $r_{\min} = 0.27\text{km}$ and $r_{\max} = 11.22\text{km}$, respectively. Figure 16b shows the distribution of the number of station pairs

as a function of the interstation spacing and azimuth. Figure 16c shows the ARF of the subarray in Figure 16a.

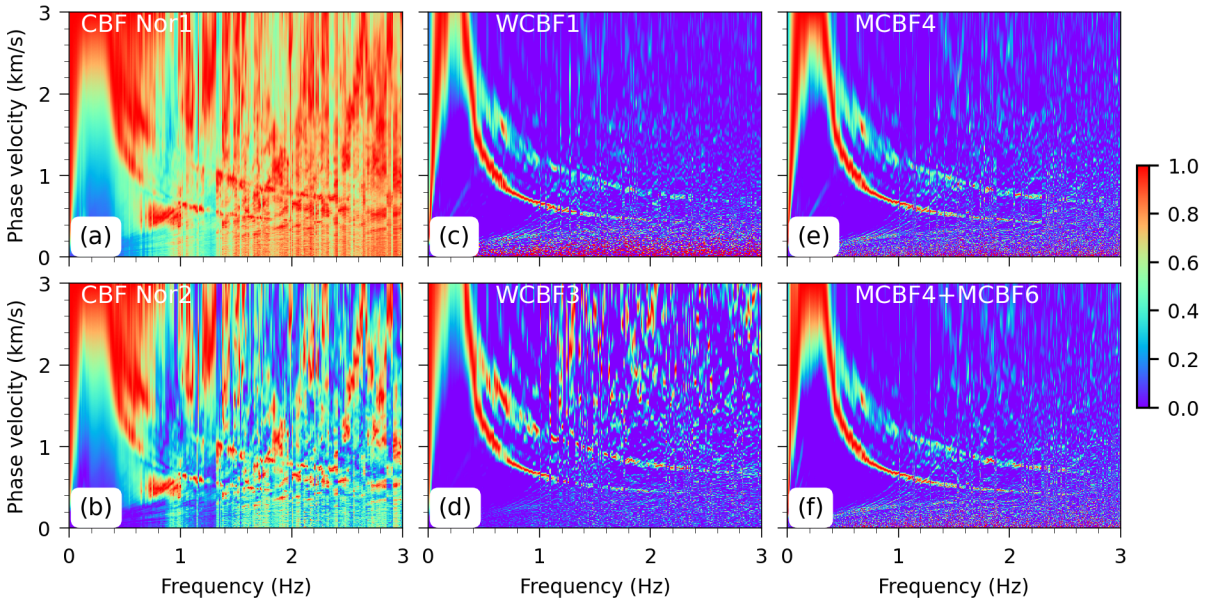

Figure 17. The dispersion image obtained by different imaging conditions for the array shown in Figure 16a. (a) and (b) are the results of CBF with the same normalization strategies as those used in Figures 1b and 1d, respectively. (c) and (d) are the results of WCBF1 and WCBF2, respectively. (e) and (f) are the results of MCBF4 and MCBF4+MCBF6. Only the positive values are color-coded in (c)-(f).

Figure 17 shows the dispersion image obtained by different imaging conditions of beamforming for the array consisting of twenty-nine stations shown in Figure 16a. Figure 17a and 17b show the results of CBF with the same normalization strategies as those used in Figure 1b and 1d, respectively. Figure 17c and 17d are the results of WCBF, where the result of WCBF3 are equivalent to that obtained by F-J method. The results of MCBF are given in Figures 17e and 17f. It can be found that in order to obtain the dispersion image with the same clarity, larger number of stations may be required for conventional CBF. Correction for wavenumber and propagation distance can significantly improve the clarity of the dispersion image. Again, consistent with the previous discussion, due to the irregular station distribution, the result of MCBF4 is similar to that of the designed anti-aliasing scheme MCBF4+MCBF6, and no obvious aliasing is observed.

6.2.2. Examples for the USArray and ChinArray at Regional Scale

The average station spacing of the above two example arrays shown in Figure 1a and Figure 16a is

about 1 km. They are subsets sampled from two dense arrays at local scale. The effective frequency range of the extracted multimode dispersion curves is about 0.3-3 Hz. Two examples for the subarray at regional scale are presented in this section.

One array is the subset sampled from USArray. Figure 18a shows the station map of this array which contains 108 stations with an average station spacing of 70 Km. A total ninety days continuous waveform recorded from 1 June 2011 to 31 August 2011 are used. Figure18b shows the dispersion image obtained by MCBF. The fundamental (mode 0) and five higher modes (modes 1-5) are clearly observed. The effective frequency range is about 0.03-0.6 Hz, depends on the mode branches. In such a relatively wide frequency band, different modes correspond to varying wavelengths and propagation velocities, as a result, the modes usually cannot be separated apparently in the time domain for the interstation NCFs (See Figure S5 in the supporting information for the interstation NCFs whithin the array). This means the mode separation in the time domain is not a requirement for extracting multimode dispersion curves using MCBF. As a comparison, the theoretical dispersion curves predicted by the reference model are presented by dashed lines. The reference model is obtained by averaging the model under the array given by Shen and Ritzwoller (2016).

Another array is the subset sampled from ChinArray (Phase II). As shown in Figure 18c, this array contains 104 stations with an average station interval of 30km. K. Wang et al. (2020) have extracted the fundamental mode Rayleigh wave between 7 and 35 s using the conventional CBF. We applied the NCFs, which are the stacking results of three months continuous records (from 1 January 2014 to 31 March 2014), to investigate the extraction of higher modes by MCBF. The resulted dispersion image is shown in Figure 18d. The white dashed lines denote the dispersion curves predicted by the averaged model under the array given by K. Wang et al. (2020). For the fundamental mode Rayleigh wave, the predicted dispersion curve agrees well with the observed one in the frequency range of 7 -35 s. This is not surprised since the model given by K. Wang et al. (2020) is derived from the inversion of the fundamental mode Rayleigh dispersion curve at this frequency rang. However, for the fundamental mode Rayleigh wave at frequencies higher than 0.14 Hz (7 s) and the higher modes, the predicted dispersion curve deviated from the observed one. This phenomenon can also be observed for the USArray shown in Figure 18b, where the predicted dispersion curves for the

higher modes and the fundamental mode with frequencies above 0.3 Hz also deviate from those observed. We inverted for a new model using extracted multimode dispersion curves. The predicted dispersion curves using the new inverted model agree well with the observed one (See Figure S6 in the supporting information for the inverted model using multimode surface wave and the corresponding predicted dispersion curves). This gives an illustration on the importance of high modes in surface wave inversion.

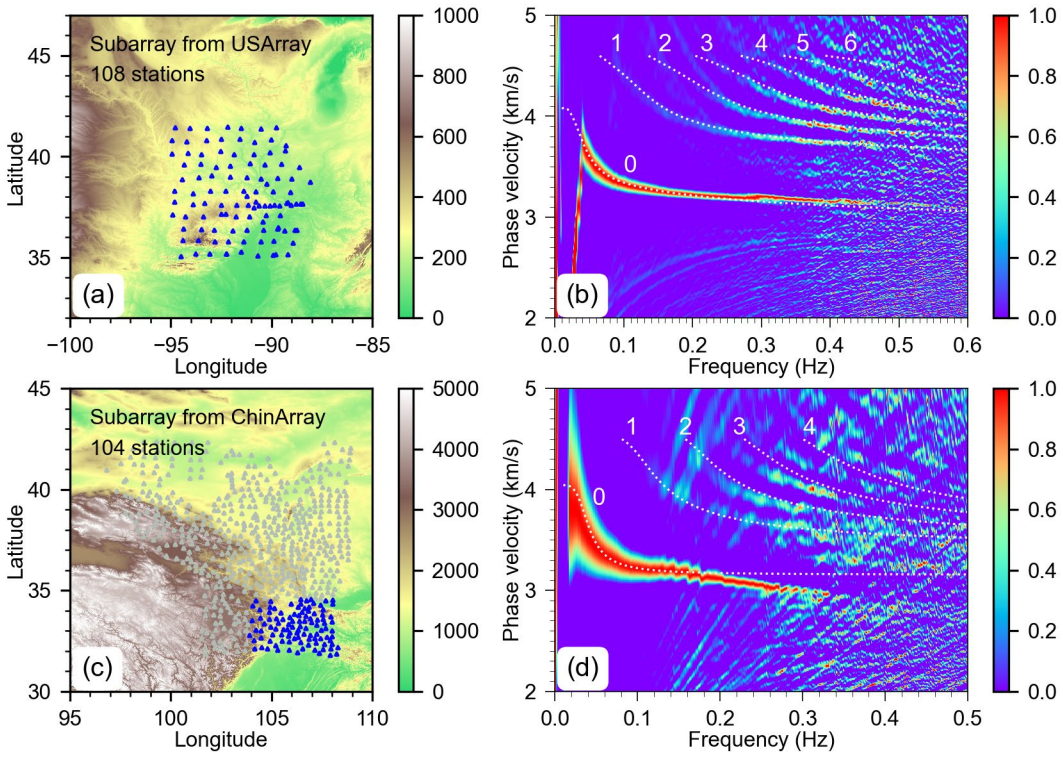

Figure 18. Two examples on the extraction of multimode dispersion curves using MCBF for the array at regional scale, whicn are the subsets of the USArray (a) and ChinArray (c), respectively. The stations inside the array used in this paper are presented by blue triangles in left panels. The corresponding dispersion images obtained by MCBF are shown in right panels. The white dashed lines in (b) are the predicted dispersion curves for the averaged model from Shen and Ritzwoller (2016). In (d), the white dashed lines are the predicted dispersion curves for the averaged model from K.Wang et al. (2020).

6.3. The Influence of the Parameters on the Results of MCBF

6.3.1. The Time Length of the Recordings

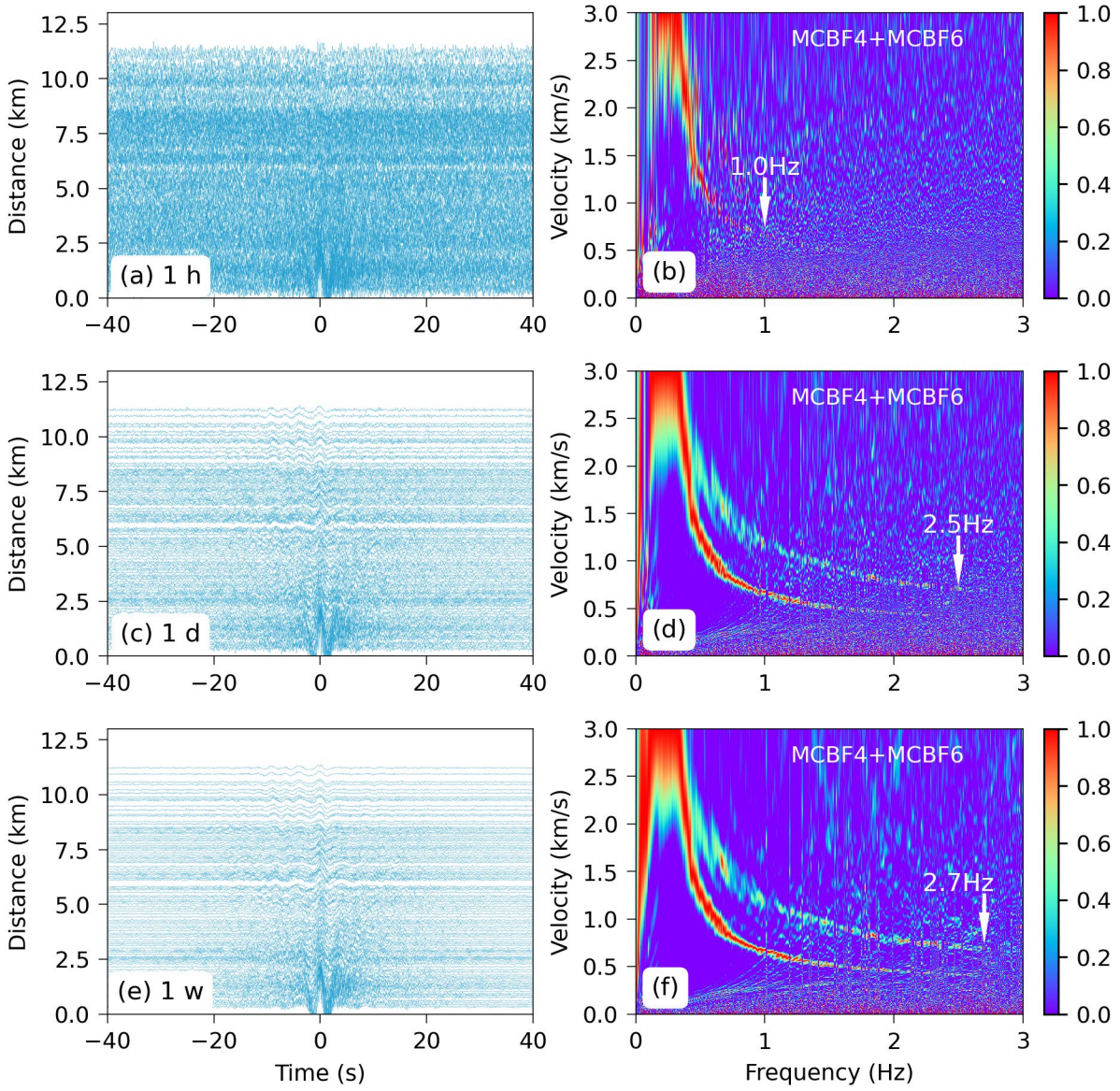

Figure 19. Bandpass (0.2-5 Hz) filtered NCFs for the interstation within the array shown in Figure 16a, which are retrieved from recording length of 1 hour (a), 1 day (c) and 1 week (e), respectively. The corresponding dispersion images obtained by MCBF are presented in right panels.

Besides the ability to extract multimode surface wave dispersion curves, another advantage of BF over traditional NCF-based methods is that phase velocities can be estimated accurately using quite shorter recordings. For the array data shown in Figure 1a, Qin et al. (2022) found that

recordings as short as a few hours to days are sufficient to extract reliable dispersion curves of the fundamental and the first higher mode between 0.3 and 1.5 Hz by CBF. This is consistent with the conclusion of Roux and Ben-Zion (2017), who estimated reliable phase velocities for the fundamental mode Rayleigh waves using the recording with similar length from California network. The same conclusion can also be obtained for MCBF for the array shown in Figure 1a (See Figures S7 and S8 in the supporting information for the corresponding results of MCBF for the array shown in Figure 1a). Furthermore, for the same recording length, the energy of the dispersion image given by MCBF is more concentrated on the dispersion branches than that given by CBF, resulting in a clean dispersion image with few artifacts (e.g., seen by comparing Figure S7 in the supporting information with Figure 7 in Qin et al. (2021)).

For the array shown in Figure 16a, we calculated the NCFs by stacking the different recording length of 1 hour, 1 day and 1 week, respectively. The bandpass (0.2-5 Hz) filtered NCFs retrieved from different recording lengths and corresponding dispersion image obtained by MCBF are presented in Figure 19. As expected, the longer the recording length, the higher the signal-to-noise ratio (SNR) of the NCFs and, correspondingly, the wider the frequency band of the dispersion curves resolved by MCBF. Also, the dispersion image looks cleaner for long time recordings due to fewer artifacts. However, the width of the energy band along two dispersion branches, which is often an indicator on the precision of the velocity measurement, does not narrow significantly as the recording length increases. This implies the recording length is not the main factor affecting the precision of velocity estimation, and it mainly control the resolved frequency band and the artifacts occurred in the image.

6.3.2. The Number of Stations

As discussed in section 2.3, for the time series with the same length, the resolved frequency band and the resolution of the dispersion measurement by BF depend on the wavefield beneath the array and ARF. The wavefield mainly depends on the complexity of the velocity structure under the array, which affects the emergence of interstation NCFs and thus the quality of the dispersion image. For real arrays with known station distribution, our main concern is the effect of ARF, which is determined by the array configuration, and thus by the array size, shape, interstation distance

and the number of stations inside the array. For the measurements of the azimuth-averaged phase velocity, or in other words, assuming the structure beneath the array does not vary with azimuth, the number of stations is a major factor affecting the measurement accuracy. This is because the algorithm in MCBF can be thought as a discrete summation of an integral with Fourier transformed NCFs as the kernel. The accuracy of the integral is determined by the number of NCFs and the intervals between them, which are mainly related to the number of stations (rather than array shape) for a given array configuration.

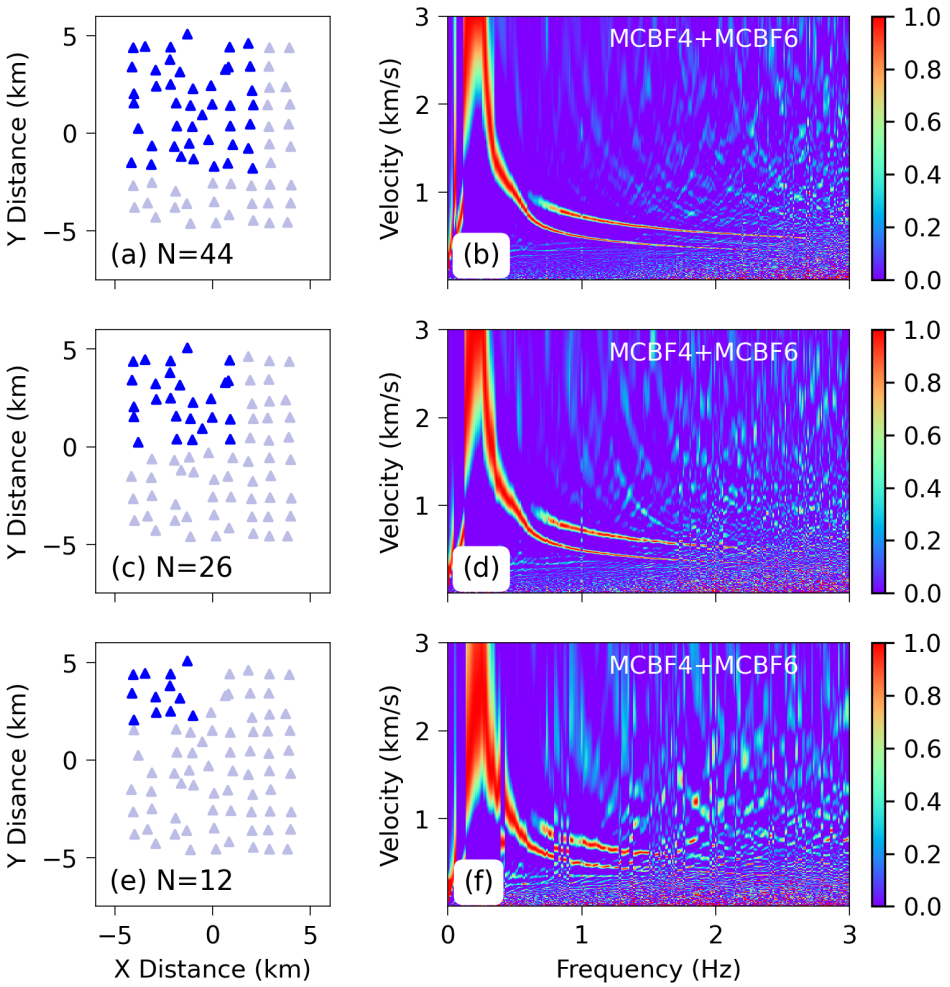

Figure 20. The dispersion images obtained by MCBF using the subsets of the stations inside the array shown in Figure 1a. The size of the subarrays represented by blue triangles in left panels are 7×7 km^2, 5×5 km^2 and 3×3 km^2. The number of stations are 44, 26 and 12, respectively. The corresponding dispersion image for these three subarrays are presented in right panels. Only the positive value is color-coded in the dispersion images (See Figure S9 in the supporting information where both the positive and negative values are color-coded).

926 The number of stations mainly depends on the size of the array if the station distribution is given.
927 Therefore, in order to ensure the accuracy of reliable dispersion measurements and sufficient
928 lateral resolution, a trade-off between the array size and the number of stations within the array
929 needs to be made when applying BF technique with moving subarrays. For the array data shown
930 in Figure 1a, Qin et al. (2022) investigated the influence of the number of stations on the estimation
931 of dispersion curves using CBF through tentative experiments and to determine the appropriate
932 size of the array. Using the same dataset, we analyze the effect of the station number on the results
933 of MCBF.

934 The array aperture in Figure 1a is about 10×10 km^2. To reduce the array size, we take the subset
935 of the stations from the upper left corner of the array to get three square subarrays with sizes of
936 7×7 km^2, 5×5 km^2 and 3×3 km^2. The station distributions of these subarrays are presented by blue
937 triangles in left panels of Figure 20. The corresponding dispersion images obtained by MCBF are
938 given in right panels of Figure 20. The number of stations of these three subarrays are 44, 26 and
939 12, respectively.

940 It can be seen from top to bottom panels in the right column of Figure 20, as the station number
941 decreases, the reliable frequency band reduces and the energy bands along the two dispersion
942 branches widen. This implies the reduction in the array size and thus the number of stations
943 resulted in a narrowing of the resolved frequency range and reduced measurement accuracy,
944 similar to the observation in Qin et al. (2022) for the results of CBF. However, compared with Figure
945 6 in Qin et al. (2022), the dispersion image given by MCBF in Figure 20 is much clearer and less
946 interference from aliasing.

947 **6.3.3. The Geometry of the Array**

948 As a function of the azimuth, the beamforming output depends on the shape of the array,
949 especially the azimuth distribution of the dominant station-pair orientation would seriously affect
950 the azimuth distribution of the beampower. However, for the azimuth-averaged velocity, the effect
951 of the array shape on the dispersion image is slight. Figure 21 shows the results of MCBF for three
952 subsets with different shape sampled from the array shown Figure 1a. The blue triangles in the left
953 panels of Figure 21 denote the station map of three subsets, which are approximately circular (a),

L-shaped (c) and linear (e), respectively. The corresponding result of MCBF for each subset is given in the panels of the right column. The energy belts along two dispersion branches can be resolved for these three subarrays. Although the reliable frequency range and resolution are slightly different. Figures 21b and 21f show that the phase velocities along two mode branches are quite similar to those obtained from square arrays in Figures 20b and 20f.

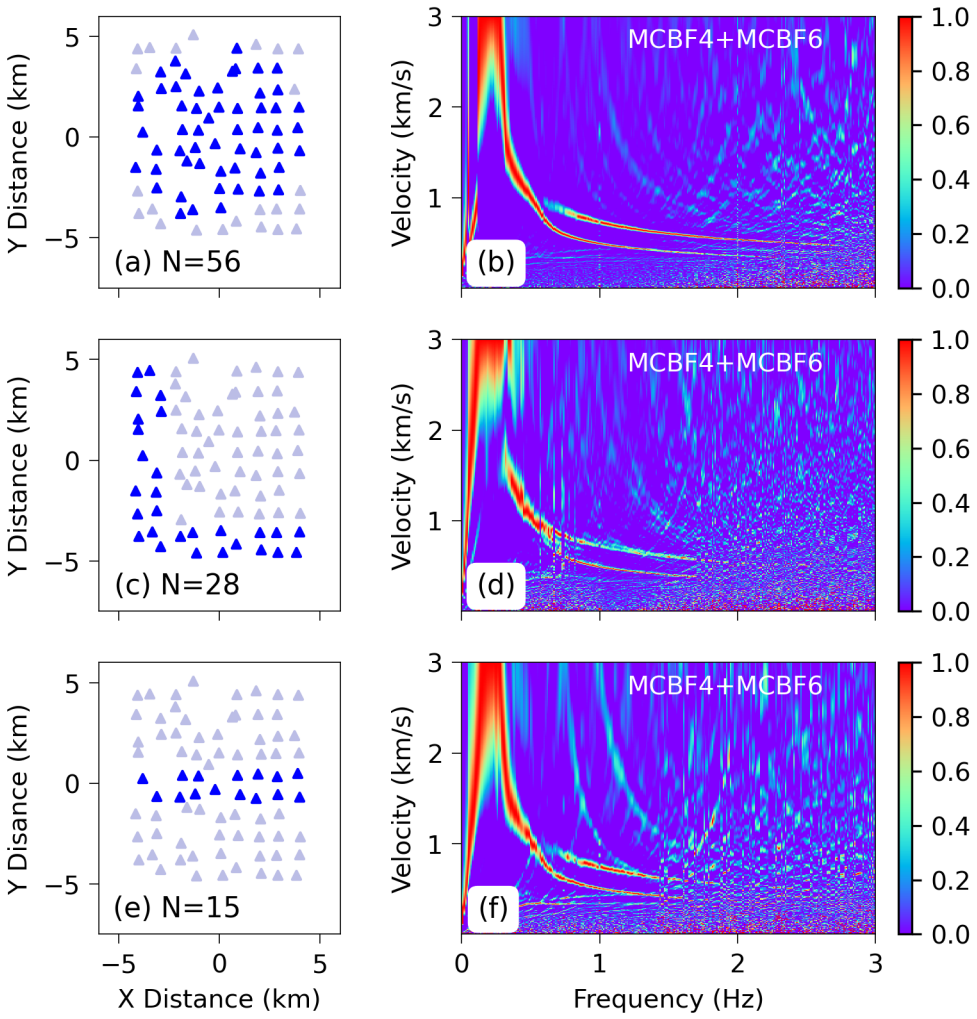

Figure 21. Dispersion images obtained by MCBF using the subsets with different shapes of the array in Figure 1a. The blue triangles in the left panels denote stations of within three subsets, which are approximately circular (a), L-shaped (c) and linear (e), respectively. The station numbers N are labeled in each panel. The corresponding result of MCBF for each subset is given in the panels of the right column. Only the positive value is color-coded in the dispersion images (See Figure S10 in the supporting information where both the positive and negative values are color-coded).

Figure 21d shows that the dispersion curve of the fundamental mode intersects that of the first higher mode at 0.6 Hz for the result of the L-shaped array, slightly different from the results of the square array shown in Figure 20. This may be due to the fact that the stations involved in the L-shaped array covers different tectonic units (Qin et al., 2022). The assumption that the model under the array is laterally isotropic does not hold any more. Generally speaking, for the extraction of azimuth-averaged velocity, the effect of the array shape on the dispersion curve is much smaller than that of the station numbers. This conclusion holds for WCBF and CBF, as well as MCBF. As for the extraction of the azimuth-dependence velocity, the shape of the array would affect the beamforming output and thus the velocity estimation for WCBF and CBF. However, the array shape does not significantly affect the results of MCBF, even for the estimation on the azimuth-dependence velocity.

7. Discussion and Conclusions

The deployment of dense array at different scale is becoming a routine operation in observational seismology. It is therefore becoming possible to directly obtain the lateral variation of the velocity under the array by applying the array-based surface wave method to the subset of the dense array through the moving window technology. As two array-based techniques for extracting multimode surface wave from noise recording, BF and F-J methods have been developed independently, based on the physical interpretations from different point of view. In this paper, the equivalence of BF and F-J methods are proved as far as their application in extracting multimode dispersion curves is concerned. The weighted (WCBF) and modified (MCBF) BF methods are proposed and their explicit relationship to the F-J method is given. For the finite sampling on spatial wavefield in practical applications, explicit theoretical representations of the BF technique are given for different imaging conditions. These representations can be used to investigate analytically the features of the dispersion image and how the aliasing is eliminated. The proposed methods are validated both for the synthetic data and the real data from the dense array at different scales. In summary, the main conclusions of this paper are as follows:

(1) For the conventional CBF, the plane wave at a given azimuth is projected into the station pairs distributed at different orientation. This operation on azimuthal average physically means that

994 the structure beneath the array are laterally uniform. Mathematically, azimuth-average would
995 express the plane waves represented by the complex exponential function $e^{ikr\cos\theta}$ as the Bessel
996 function $J_0(kr)$, which results in an additional geometric spread factor of $1/\sqrt{kr}$ and $-\pi/4$
997 phase shift (i.e., the difference of the far field approximation of $J_0(kr)$ and cosine function
998 $\cos(kr)$).

999 (2) Considering the fact mentioned in (1), WCBF is proposed to correct the geometric spread factor
1000 (Since the NCF also has $-\pi/4$ phase shift relative to the plane wave, the phase correction is
1001 not needed in WCBF). By comparing the operation on the projection of plane waves in WCBF
1002 and the integration with kernel of $J_0(kr)$ in F-J, it is found the WCBF is equivalent to F-J,
1003 differing by a factor $1/k$. This means the assumption that the structure under the array is
1004 laterally homogeneous is also made in F-J method. The F-J transform is theoretically 2D Fourier
1005 transform of the radially symmetric function. The velocity obtained by WCBF and F-J is the
1006 azimuth-averaged result. The subtle differences in the azimuth-averaged velocities obtained
1007 by BF and F-J may originate from the strategy for numerical calculation. If WCBF and F-J are
1008 used to extract the azimuth-dependence velocity, for instance, by picking the azimuth-
1009 dependence maximum of the beampower in WCBF or by considering only the NCFs at expected
1010 azimuth in F-J, the errors caused by the array geometry is inevitable.

1011 (3) Since both WCBF and F-J assume that there is no lateral variation in the velocity structure under
1012 the array, we proposed a MCBF scheme in which the projection of the plane waves into the
1013 station pairs is omitted. For a given station pair, only the incident plane wave that is consistent
1014 with its orientation is considered in MCBF. For the azimuth-averaged velocity, the dispersion
1015 image with the same even high resolution as that given by WCBF and F-J can be obtained by
1016 MCBF. Furthermore, in contrast to WCBF and F-J, azimuth-dependence velocity can also be
1017 measured by MCBF independent of the array geometry theoretically. The explicit relationship
1018 between the azimuth-averaged MCBF and F-J is given.

1019 (4) For an ideal cylindrical wavefield, the theoretical representations of MCBF for different imaging
1020 conditions are derived for the finite spatial sampling. The beamforming output of the MCBF for

the imaging conditions with sine and cosine functions as the basis function can be expressed as the summation of the products between trigonometric and sinc functions with the arguments $k_n - k$ and $k_n + k$. The characteristic wavenumbers k_n and aliasing wavenumbers $-k_n$ are associated with the maximum, or the zero-crossing points between two peaks of the beampower, depending on the choice of the basis function. The beamforming output contains the items only with the argument $k_n - k$ or $k_n + k$ can be achieved by the linear combination of different imaging condition. The aliasing wavenumbers can thus be separated and removed.

(5) The validity of the proposed methods is illustrated by synthetic data and the data of the dense array at different scales. For the azimuth-averaged velocity, the results are less affected by the array geometry, both for WCBF and MCBF. The resolution and reliable frequency range of the dispersion image are controlled mainly by the number of stations, which depends on the array size and interstation spacing. In addition, the dispersion curves can be estimated with adequate accuracy using quite short recordings, for instance over a few hours to days. This offers the possibility on the rapid assessment of the medium properties.

Data Availability Statement

The waveform data of USArray were obtained from the website (https://ds.iris.edu/ds/nodes/dmc/data/types/waveform-data). The NCFs of the ChinArray (Phase II) for the stations used in the paper can be found at https://doi.org/10.6084/m9.figshare.20304618.v1. The NCFs of two dense arrays at local scale used as the examples in this paper, as well as the Python package for generating the dispersion image using different BF schemes based on these NCFs, are also openly available from https://doi.org/10.6084/m9.figshare.20304618.v1.

Acknowledgments

This work was supported by the National Natural Science Foundation of China (U1839209) and the National Key R & D Program of China (2017YFC1500200).

Appendix A: Convention for the Fourier transform, Hilbert transform and cross-correlation

The following convention for Fourier transform from the time (t) domain to the frequency (ω) domain is adopted in this paper.

$$f(t)=\int_{-\infty}^{\infty}F(\omega)e^{i\omega t}d\omega$$
$$F(\omega)=\frac{1}{2\pi}\int_{-\infty}^{\infty}f(t)e^{-i\omega t}dt \quad \text{(A1)}$$

Accordingly, for the Fourier transform from the space (r) domain to the wavenumber domain (k) we use the convention

$$f(r)=\int_{-\infty}^{\infty}F(k)e^{-ikr}dk$$
$$F(k)=\frac{1}{2\pi}\int_{-\infty}^{\infty}f(r)e^{ikr}dr \quad \text{(A2)}$$

$f(t)$ and $F(\omega)$, as well as $f(r)$ and $F(k)$ are two Fourier transform pairs. These conventions imply the plane wave expression $e^{-ikx}e^{i\omega t}$ describes the wave propagating in the positive x, while $e^{+ikx}e^{i\omega t}$ describes the wave propagating in the negative x. For the cylindrical wave in the Cartesian coordinate system with z downwards, the zero-order Hankel function $H_0^{(1)}(kr)$ of the first kind represents the converging wave and the zero-order Hankel function $H_0^{(2)}(kr)$ of the second kind represents the wave propagating outwards.

The Hilbert transform of the function $s(x)$ is defined as

$$s(t)=\mathcal{H}\,[s(x)]=\frac{1}{\pi}\mathrm{P.V.}\int_{-\infty}^{+\infty}\frac{s(x)}{t-x}d\tau \quad \text{(A3)}$$

where P.V. represents the principal value of the Cauchy integral. Under this definition, the analytical signal $S(t)$ of the real-value signal $s(t)$ can be expressed as

$$S(t)=s(t)+i\mathcal{H}\,[s(t)] \quad \text{(A4)}$$

The symbol $\mathcal{H}$ represents the Hilbert transform.

The cross-correlation of two (complex) signals is defined as

$$C_{fg}(\tau)=\int_{-\infty}^{+\infty}f^{*}(t)g(t+\tau)dt \quad \text{(A5)}$$

where superscript * represents complex conjugate. If the Fourier transform of $g(t)$ is $G(\omega)$. According to this definition and the above convention for Fourier transform, we have

$$C_{fg}(\tau)=\frac{1}{2\pi}\int_{-\infty}^{+\infty}F^{*}(\omega)G(\omega)e^{i\omega\tau}d\omega \quad \text{(A6)}$$

1069 i.e. $C_{fg}(\tau)$ and $F^*(\omega)G(\omega)$ are Fourier transform pair. Cross-correlation in the time domain

1070 corresponds to the product in the frequency domain by taking complex conjugate of one of them.

1071 **Appendix B: Theoretical Representation of MCBF**

1072 For an ideal cylindrical wavefield, substituting $C(r,\omega)=J_0(k_n r)$ into Equation 30. The azimuth-

1073 averaged MCBF can be written as

1074
$$\begin{aligned}\overline{MCBF}(k,\omega) &= \frac{1}{N^2}\sum_i^N\sum_j^N \sqrt{\pi k r_{ij}}\,J_0\left(k_n r_{ij}\right)e^{\imath\left(kr_{ij}-\frac{\pi}{4}\right)} \\ &= \frac{\sqrt{2}}{N^2}\frac{\sqrt{k}}{\sqrt{k_n}}\left(\sum_i^N\sum_j^N \cos\left(k_n r_{ij}-\frac{\pi}{4}\right)e^{\imath\left(kr_{ij}-\frac{\pi}{4}\right)}\right)\end{aligned} \tag{B1}$$

1075 In Equation B1, the far field approximation of $J_0(k_n r)$ shown in Equation 20 is applied. The double

1076 summation over the number of stations means the summation over the interstation distance r_{ij}.

1077 Since the geometric spread is corrected by multiplying r_{ij} in Equation B1, the autocorrelation for

1078 $i=j$ is excluded. The cross-correlations for $i\neq j$ are counted twice for the same interstation

1079 distance $r_{ij}=r_{ji}$. Equation B1 can then be written as

1080
$$\begin{aligned}\overline{MCBF}(k,\omega) &= \frac{2\sqrt{2}}{N^2}\frac{\sqrt{k}}{\sqrt{k_n}}\sum_j^M \cos(k_n r_j-\frac{\pi}{4})e^{i(kr_j-\frac{\pi}{4})} \\ &= \frac{2\sqrt{2}}{N^2}\frac{\sqrt{k}}{\sqrt{k_n}}\sum_j^M \cos(k_n r_j-\frac{\pi}{4})\left(\cos(kr_j-\frac{\pi}{4})+i\sin(kr_j-\frac{\pi}{4})\right)\end{aligned} \tag{B2}$$

1081 where $M=N(N-1)/2$. Let

1082
$$CC=\sum_j^M \cos(k_n r_j-\frac{\pi}{4})\cos(kr_j-\frac{\pi}{4})=\frac{1}{2}\sum_j^M\left[\cos(k_n r_j-kr_j)+\sin(k_n r_j+kr_j)\right] \tag{B3}$$

1083 It is assumed the cylindrical wavefield is sampled spatially in radial distance with equal interval Δr.

1084 We have $r_j=j\Delta r$. Equation B3 can be rewritten as

1085
$$CC=\frac{1}{2}\sum_j^M\left[\cos(k_n-k)j\Delta r+\sin(k_n+k)j\Delta r\right] \tag{B4}$$

1086 Applying the Equations 1.342.1 and 1.342.2 in Gradshteyn and Ryzhik (2007,P37)

$$\sum_{k=0}^{n}\cos kx=\cos\tfrac{n+1}{2}x\frac{\sin\frac{nx}{2}}{\sin\frac{x}{2}}+1$$
$$\sum_{k=1}^{n}\sin kx=\sin\tfrac{n+1}{2}x\frac{\sin\frac{nx}{2}}{\sin\frac{x}{2}} \tag{B5}$$

Equation B4 can be recast into

$$\begin{aligned}CC&=\frac{1}{2}\left[\cos\tfrac{(M+1)(k_n-k)\Delta r}{2}\frac{\sin\frac{M(k_n-k)\Delta r}{2}}{\sin\frac{(k_n-k)\Delta r}{2}}+\sin\tfrac{(M+1)(k_n+k)\Delta r}{2}\frac{\sin\frac{M(k_n+k)\Delta r}{2}}{\sin\frac{(k_n+k)\Delta r}{2}}\right]\\&=\frac{M}{2}\left[\cos\tfrac{(M+1)(k_n-k)\Delta r}{2}D_M\left(\tfrac{(k_n-k)\Delta r}{2}\right)+\sin\tfrac{(M+1)(k_n+k)\Delta r}{2}D_M\left(\tfrac{(k_n+k)\Delta r}{2}\right)\right]\end{aligned} \tag{B6}$$

where

$$D_M(x)=\frac{\sin\frac{Mx}{2}}{M\sin\frac{x}{2}} \tag{B7}$$

is the Dirichlet sinc function. For a small Δr and large M, we have $\sin\Delta r=\Delta r$, $R=M\Delta r\approx(M+1)\Delta r$. Equation B6 can be approximately expressed as

$$CC\approx\frac{M}{2}\left[\cos\tfrac{R(k_n-k)}{2}\operatorname{sinc}\tfrac{R(k_n-k)}{2}+\sin\tfrac{R(k_n+k)}{2}\operatorname{sinc}\left(\tfrac{R(k_n+k)}{2}\right)\right] \tag{B8}$$

where $\operatorname{sinc}(x)=\sin x/x$ is the sinc function. Similarly, it can be deduced

$$\begin{aligned}CS&=\sum_j^M\cos(k_nr_j-\frac{\pi}{4})\sin(kr_j-\frac{\pi}{4})=\frac{1}{2}\sum_j^M\left[\cos(k_nr_j+kr_j)-\sin(k_nr_j-kr_j)\right]\\&=\frac{M}{2}\left[\cos\tfrac{(M+1)(k_n+k)\Delta r}{2}D_M\left(\tfrac{(k_n+k)\Delta r}{2}\right)-\sin\tfrac{(M+1)(k_n-k)\Delta r}{2}D_M\left(\tfrac{(k_n-k)\Delta r}{2}\right)\right]\\&\approx\frac{M}{2}\left[\cos\tfrac{R(k_n+k)}{2}\operatorname{sinc}\tfrac{R(k_n+k)}{2}-\sin\tfrac{R(k_n-k)}{2}\operatorname{sinc}\left(\tfrac{R(k_n-k)}{2}\right)\right]\end{aligned} \tag{B9}$$

$$\begin{aligned}SS&=\sum_j^M\sin(k_nr_j-\frac{\pi}{4})\sin(kr_j-\frac{\pi}{4})=\frac{1}{2}\sum_j^M\left[\cos(k_nr_j-kr_j)-\sin(k_nr_j+kr_j)\right]\\&=\frac{M}{2}\left[\cos\tfrac{(M+1)(k_n-k)\Delta r}{2}D_M\left(\tfrac{(k_n-k)\Delta r}{2}\right)-\sin\tfrac{(M+1)(k_n+k)\Delta r}{2}D_M\left(\tfrac{(k_n+k)\Delta r}{2}\right)\right]\\&\approx\frac{M}{2}\left[\cos\tfrac{R(k_n-k)}{2}\operatorname{sinc}\tfrac{R(k_n-k)}{2}-\sin\tfrac{R(k_n+k)}{2}\operatorname{sinc}\left(\tfrac{R(k_n+k)}{2}\right)\right]\end{aligned} \tag{B10}$$

The modulus of $CC+iCS$ can be approximated as

$$\left|CC+iCS\right|=\frac{\sqrt{2}}{N^2}\frac{\sqrt{k}}{\sqrt{k_n}}\left(\operatorname{sinc}\frac{R(k_n+k)}{2}+\operatorname{sinc}\frac{R(k_n-k)}{2}\right) \tag{B11}$$

We therefore have

1101 $$\overline{MCBF}(k,\omega)=\frac{\sqrt{2}}{N^2}\frac{\sqrt{k}}{\sqrt{k_n}}\left[CC+iCS\right] \tag{B12}$$

1102 The theoretical representations of the azimuth-averaged MCBF with different imaging conditions
1103 can then be written as

$$MCBF1=\frac{\sqrt{2}M}{N^2}\frac{\sqrt{k}}{\sqrt{k_n}}\left(\cos\frac{R(k_n-k)}{2}\operatorname{sinc}\frac{R(k_n-k)}{2}+\sin\frac{R(k_n+k)}{2}\operatorname{sinc}\frac{R(k_n+k)}{2}\right)$$
$$MCBF2=\frac{\sqrt{2}M}{N^2}\frac{\sqrt{k}}{\sqrt{k_n}}\left|\cos\frac{R(k_n-k)}{2}\operatorname{sinc}\frac{R(k_n-k)}{2}+\sin\frac{R(k_n+k)}{2}\operatorname{sinc}\frac{R(k_n+k)}{2}\right|$$
$$MCBF3=\frac{\sqrt{2}}{N^2}\frac{\sqrt{k}}{\sqrt{k_n}}\left(\operatorname{sinc}\frac{R(k_n+k)}{2}+\operatorname{sinc}\frac{R(k_n-k)}{2}\right)$$
$$MCBF4=MCBF1$$
$$MCBF5=\frac{\sqrt{2}M}{N^2}\frac{\sqrt{k}}{\sqrt{k_n}}\left(\cos\frac{R(k_n+k)}{2}\operatorname{sinc}\frac{R(k_n+k)}{2}-\sin\frac{R(k_n-k)}{2}\operatorname{sinc}\frac{R(k_n-k)}{2}\right)$$
$$MCBF6=\frac{\sqrt{2}M}{N^2}\frac{\sqrt{k}}{\sqrt{k_n}}\left(\cos\frac{R(k_n-k)}{2}\operatorname{sinc}\frac{R(k_n-k)}{2}-\sin\frac{R(k_n+k)}{2}\operatorname{sinc}\frac{R(k_n+k)}{2}\right)$$
$$MCBF4+MCBF6=\frac{2\sqrt{2}M}{N^2}\frac{\sqrt{k}}{\sqrt{k_n}}\cos\frac{R(k_n-k)}{2}\operatorname{sinc}\frac{R(k_n-k)}{2}$$
$$MCBF4-MCBF6=\frac{2\sqrt{2}M}{N^2}\frac{\sqrt{k}}{\sqrt{k_n}}\sin\frac{R(k_n+k)}{2}\operatorname{sinc}\frac{R(k_n+k)}{2}$$

1104 (B13)

1105 Theoretically, MCBF1 is equivalent to MCBF4. However, in practice, the cross spectrum $C(r,\omega)$,
1106 i.e., the Fourier transform of NCFs is usually complex rather than the perfect Bessel function $J_0(kr)$.
1107 We therefore define MCBF1 and MCBF4 with $C(r,\omega)$ and $\mathrm{Re}\left[C(r,\omega)\right]$, respectively.

1108 **References**

1109 Aki, K. (1957). Space and Time Spectra of Stationary Stochastic Waves, with Special Reference to Microtremors.
1110 *Bulletin of the Earthquake Research Institute*, *35*, 415–456.

1111 Asten, M. W., & Henstridge, J. D. (1984). Array estimators and the use of microseisms for reconnaissance of
1112 sedimentary basins. *Geophysics*, *49*(11), 1828–1837. https://doi.org/10/cv83cb

1113 Baddour, N. (2011). Chapter 1 - Two-Dimensional Fourier Transforms in Polar Coordinates. In P. W. Hawkes (Ed.),
1114 *Advances in Imaging and Electron Physics* (Vol. 165, pp. 1–45). Elsevier. https://doi.org/10.1016/B978-0-12-
1115 385861-0.00001-4

1116 Ben-menahem, A., & Singh, S. J. (1968). Multipolar elastic fields in a layered half space. *Bulletin of the*
1117 *Seismological Society of America*, *58*, 1519–1572.

Campillo, M., & Paul, A. (2003). Long-Range Correlations in the Diffuse Seismic Coda. *Science*, *299*(5606), 547–549. https://doi.org/10.1126/science.1078551

Capon, J. (1969). High-resolution frequency-wavenumber spectrum analysis. *Proceedings of the IEEE*, *57*(8), 1408–1418. https://doi.org/10/ccpxt7

Chávez-García, F. J., & Luzón, F. (2005). On the correlation of seismic microtremors. *Journal of Geophysical Research: Solid Earth*, *110*(B11). https://doi.org/10.1029/2005JB003671

Chen, Xiaofei, (1999). Seismogram Synthesis in Multi-layered Half-space Part Ⅰ. Theoretical Formulations. *Earthquake Research in China*, *0*(2), 53–78.

Forbriger, T. (2003). Inversion of shallow-seismic wavefields: I. Wavefield transformation. *Geophysical Journal International*, *153*(3), 719–734.

Gal, M., Reading, A. M., & Ellingsen, S. P. (2019). Short Timescale Analysis of Microseisms and Application to Array Calibration. *Journal of Geophysical Research: Solid Earth*, *124*(3), 2684–2701. https://doi.org/10.1029/2018JB016959

Gerstoft, P., & Tanimoto, T. (2007). A year of microseisms in southern California. *Geophysical Research Letters*, *34*(20). https://doi.org/10/d2sts6

Gradshteyn, I. S. & Ryzhik, I. M. (2007). Table of Integrals, Series, and Products, Academic Press, Elsevier Inc.

Harkrider, D. G. (1964). Surface waves in multilayered elastic media I. Rayleigh and Love waves from buried sources in a multilayered elastic half-space. *Bulletin of the Seismological Society of America*, *54*(2), 627–679.

Harmon, N., Gerstoft, P., Rychert, C. A., Abers, G. A., Cruz, M. S. de la, & Fischer, K. M. (2008). Phase velocities from seismic noise using beamforming and cross correlation in Costa Rica and Nicaragua. *Geophysical Research Letters*, *35*(19). https://doi.org/10/cjgfrp

Horike, M. (1985). Inversion of Phase Velocity of Long-Period Microtremors to the S-Wave-Velocity Structure down to the Basement in Urbanized Areas. *Journal of Physics of the Earth*, *33*(2), 59–96. https://doi.org/10/fgpmkc

Hu, S., Luo, S., & Yao, H. (2020). The Frequency-Bessel Spectrograms of Multicomponent Cross-Correlation Functions From Seismic Ambient Noise. *Journal of Geophysical Research: Solid Earth*, *125*(8). https://doi.org/10.1029/2020JB019630

Lacoss, R. T., Kelly, E. J., & Toksöz, M. N. (1969). Estimation Of Seismic Noise Structure Using Arrays. *Geophysics*, *34*(1), 21–38. https://doi.org/10.1190/1.1439995

Lobkis, O. & Weaver, R. (2001). On the emergence of the Green's function in the correlations of a diffuse field. *J. Acoust. Soc. Am.*, 110:3011–3017. https://doi.org/10.1121/1.1417528

Löer, K., Riahi, N., & Saenger, E. H. (2018). Three-component ambient noise beamforming in the Parkfield area. *Geophysical Journal International*, *213*(3), 1478–1491. https://doi.org/10.1093/gji/ggy058

Lu, L. (2021). Revisiting the cross-correlation and SPatial AutoCorrelation (SPAC) of the seismic ambient noise based on the plane wave model. *Reviews of Geophysics and Planetary Physics*, *52*(2): 123-163

Lu, L., Wang, K., & Ding, Z. (2018). Effect of uneven noise source and/or station distribution on estimating the azimuth anisotropy of surface waves. *Earthquake Science*, *31*(04), 175–186.

Morse, P. M. & Feshbach, H. (1953). Methods of Theoretical Physics, McGraw-Hill Book Comp., Inc., New York, Toronto, London

Picozzi, M., Parolai, S., & Bindi, D. (2010). Deblurring of frequency-wavenumber images from small-scale seismic arrays. *Geophysical Journal International*, *181*(1), 357–368. https://doi.org/10.1111/j.1365-246X.2009.04471.x

Qin, T., Lu, L., Ding, Z., Feng, X., & Zhang, Y. (2022). High-Resolution 3D Shallow S Wave Velocity Structure of Tongzhou, Subcenter of Beijing, Inferred From Multimode Rayleigh Waves by Beamforming Seismic Noise at a Dense Array. *Journal of Geophysical Research: Solid Earth*, *127*(5), e2021JB023689. https://doi.org/10.1029/2021JB023689

Riahi, N., & Saenger, E. H. (2014). Rayleigh and Love wave anisotropyin Southern California using seismic noise, *Geophys. Res. Lett.*, 41, 363–369,doi:10.1002/2013GL058518.

Rost, S., & Thomas, C. (2002). ARRAY SEISMOLOGY: METHODS AND APPLICATIONS. https://doi.org/10/dt7j2t

Roux, P., & Ben-Zion, Y. (2017). Rayleigh phase velocities in Southern California from beamforming short-duration ambient noise. *Geophysical Journal International*, *211*(1), 450–454. https://doi.org/10/gb3bkc

Ruigrok, E., Gibbons, S., & Wapenaar, K. (2017). Cross-correlation beamforming. *Journal of Seismology*, *21*(3), 495–508. https://doi.org/10.1007/s10950-016-9612-6

Seydoux, L., de Rosny, J. & Shapiro, N.M. (2017). Pre-processing ambient noise cross-correlations with equalizing the covariance matrix eigenspectrum, *Geophys. J. Int.*, 210(3), 1432–1449

Shen, W., and M. H. Ritzwoller (2016), Crustal and uppermost mantle structure beneath the United States, J. Geophys. Res. Solid Earth, 121, 4306–4342, doi:10.1002/2016JB012887.

Smith, M. L. & Dahlen, F. A. (1973). The azimuth dependence of love and rayeigh wave propagation in a slightly anisotropic medium. *J. Geophys. Res.*, 78(17):3321-3333.

Tokimatsu, K. (1997). Geotechnical site characterization using surface waves. In: Ishihara (ed). Proc. 1st Intl. Conf. Earthquake eotechnical Engineering, Vol 3, Balkema, pp 1333–1368

Tsai, V. C. & Moschetti, M. P. (2010). An explicit relationship between time-domain noise correlation and spatial autocorrelation (SPAC) results. *Geophys.J.Int.*, 182(1)： 454-460 .

Wang, J., Wu, G., & Chen, X. (2019). Frequency-Bessel Transform Method for Effective Imaging of Higher-Mode Rayleigh Dispersion Curves From Ambient Seismic Noise Data. *Journal of Geophysical Research: Solid Earth*, *124*(4), 3708–3723. https://doi.org/10/gmhv6v

Wang, K., Lu, L., Maupin, V., Ding, Z., Zheng, C., & Zhong, S. (2020). Surface Wave Tomography of Northeastern Tibetan Plateau Using Beamforming of Seismic Noise at a Dense Array. *Journal of Geophysical Research: Solid Earth*, *125*(4), e2019JB018416. https://doi.org/10/ghq5kq

Wathelet, M., Jongmans, D., Ohrnberger, M., & Bonnefoy-Claudet, S. (2008). Array performances for ambient vibrations on a shallow structure and consequences over Vsinversion. *Journal of Seismology*, *12*(1), 1–19. https://doi.org/10/bwd9nr

Woods, J. W., & Lintz, P. R. (1973). Plane waves at small arrays. *GEOPHYSICS*, *38*(6), 1023–1041. https://doi.org/10/b58sts

Xi, C., Xia, J., Mi, B., Dai, T., Liu, Y., & Ning, L. (2021). Modified frequency–Bessel transform method for dispersion imaging of Rayleigh waves from ambient seismic noise. *Geophysical Journal International*, *225*(2), 1271–1280. https://doi.org/10/gh7c26

Xia, J., Miller, R. D., Park, C. B., & Tian, G. (2003). Inversion of high frequency surface waves with fundamental and higher modes. *Journal of Applied Geophysics*, *52*(1), 45–57. https://doi.org/10.1016/S0926-9851(02)00239-2

Yamaya, L., Mochizuki, K., Akuhara, T., & Nishida, K. (2021). Sedimentary Structure Derived From Multi-Mode Ambient Noise Tomography With Dense OBS Network at the Japan Trench. *Journal of Geophysical Research: Solid Earth*, *126*(6). https://doi.org/10.1029/2021JB021789

Yokoi, T. and Margaryan, S. (2008). Consistency of the spatial autocorrelation method with seismic interferometry and its consequence. *Geophysical Prospecting*, 56: 435–451.

Zhou, J., & Chen, X. (2021). Removal of Crossed Artifacts from Multimodal Dispersion Curves with Modified Frequency–Bessel Method. *Bulletin of the Seismological Society of America*. https://doi.org/10/gmr5sx